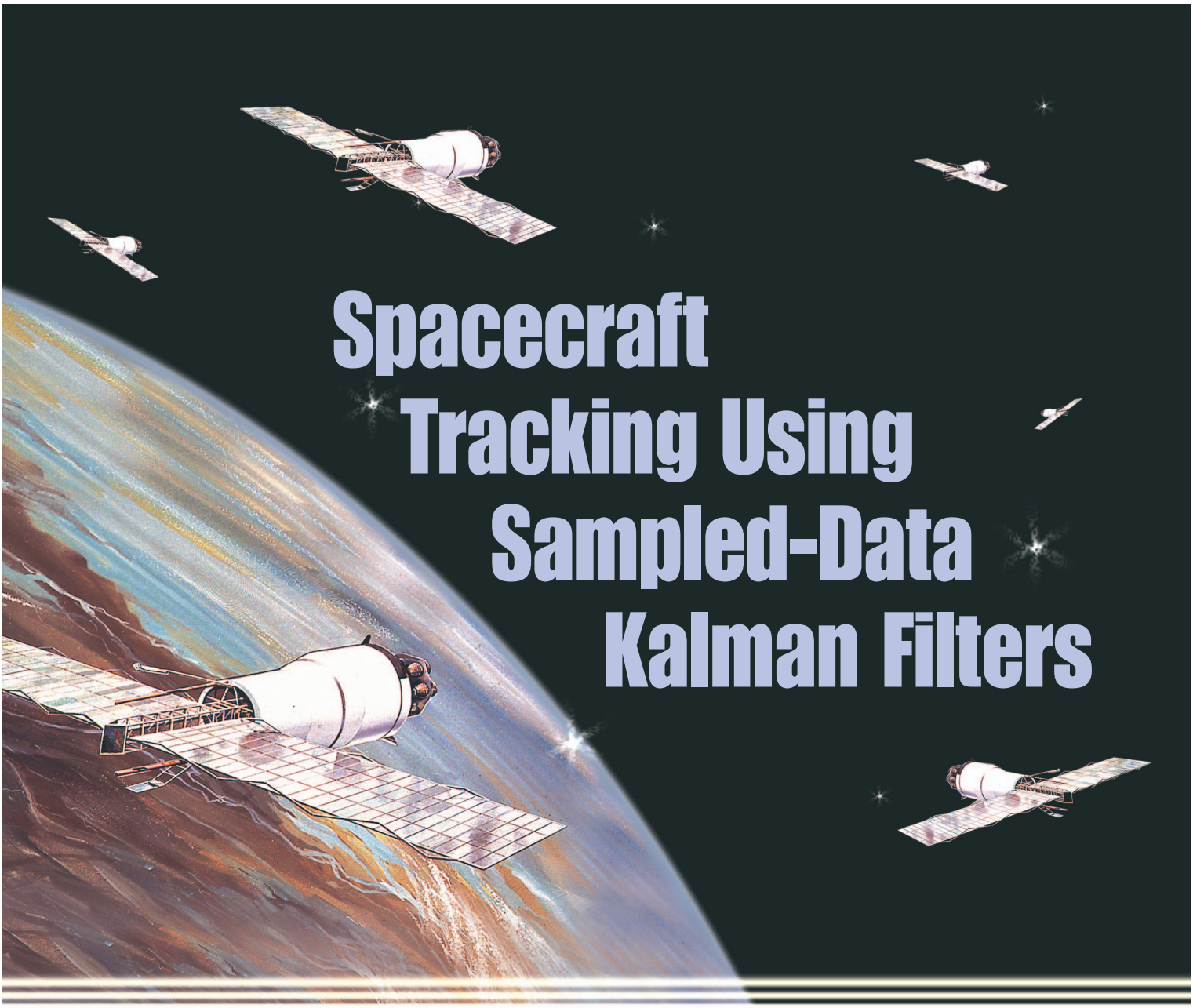

Spacecraft Tracking Using Sampled-Data Kalman Filters

NASA MARSHALL SPACE FLIGHT CENTER (NASA-MSFC)

AN ILLUSTRATIVE APPLICATION OF EXTENDED AND UNSCENTED ESTIMATORS

BRUNO O.S. TEIXEIRA,
MARIO A. SANTILLO,
R. SCOTT ERWIN, and
DENNIS S. BERNSTEIN

The problem of estimating the state of a dynamical system based on limited measurements arises in many applications. For the case of a linear system with known dynamics and Gaussian noise, the classical Kalman filter (KF) provides the optimal solution [1], [2]. However, state estimation for nonlinear systems remains a challenging problem of intense research interest. Optimal nonlinear filters [3] are often infinite dimensional and thus are difficult to implement [4]. Within a deterministic setting, nonlinear observers are available for systems of special structure [5], [6]. Except for systems of special structure, however, approximate filters are usually implemented in practice.

Two main approaches are available for approximate nonlinear filtering. The first approach is based on analytically or numerically linearizing the nonlinear dynamics and

Digital Object Identifier 10.1109/MCS.2008.923231

1066-033X/08/$25.00©2008IEEE

measurement map and then employing the classical KF equations. For example, the extended KF (EKF) [1], [2] uses nonlinear dynamics to propagate the state estimate as well as the Jacobians of the dynamics and output maps to propagate the pseudo error covariance. The EKF is often highly effective, and documented applications cover an extraordinarily broad range of disciplines, from motor control [7] to weather forecasting [8].

The second approach to approximate nonlinear state estimation uses a collection of state samples to approximate the state estimate and its error covariance. These *particle-filter* approaches include the unscented KF (UKF) [14]–[16] and ensemble [17], [18] KFs. In particular, the UKF does not propagate the error covariance (or pseudo error covariance) using a Riccati equation but rather deterministically constructs the covariance by combining a collection of state-estimate samples.

Sufficient conditions on the initial estimation error and noise properties that guarantee that the estimation error is exponentially bounded in mean square are given for EKF in [9]–[11] and UKF in [12] and [13]. Although conditions that ensure stability and convergence are often conservative for specific applications, these results provide a rationale for the EKF and UKF formalisms.

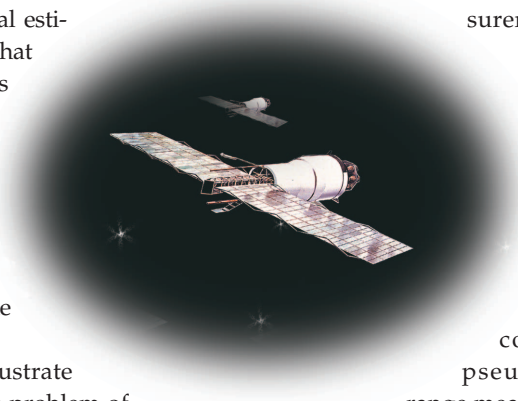

The goal of this article is to illustrate and compare EKF and UKF for the problem of satellite trajectory estimation, also known as orbit determination [19]. Various problems and alternative formulations can be considered for orbit determination based on the number and type of available measurements, including range, range rate, and angle (azimuth and elevation). The orbital dynamics of each body can be formulated either in terms of the six orbital parameters or the three instantaneous positions and three instantaneous velocities along the orbit. The differential equations for the orbital parameters can be found, for example, in [20, pp. 273–307]. These equations are singular, however, for the basic case of circular orbits due to division by the eccentricity. For orbits that are constant over long periods of time, static parameter estimation can alternatively be used to estimate the piecewise constant orbital parameters, although the complexity of the resulting nonlinear programming problem is an open question. In the present article, we adopt the Cartesian formulation due to its simplicity in deriving and applying estimation methods formulated in terms of continuous-time differential equations. The resulting problem provides a benchmark test of nonlinear estimation algorithms, which is our principal motivation for this study.

Since the orbital dynamics and the measurement map are nonlinear, nonlinear estimation techniques are needed. In addition, since measurements are available with a specified sample interval, we consider the sampled-data EKF (SDEKF) of [2, p. 188] and the sampled-data UKF (SDUKF) of [16] as approximate solutions to the spacecraft trajectory estimation problem.

Range-only orbit determination is considered in [21] and [22] using least-squares approaches and orbital-element state representations. The use of angle-only data is considered in [23], which develops a specialized filter to exploit the monotonicity of angles in orbital motion. Orbit determination using range and angle measurements from a fixed-location radar tracking system is considered in [24], where UKF is found to have improved performance relative to EKF in relation to initialization with clustered measurements available during a limited portion of each satellite pass. Issues that arise in the use of range-rate (Doppler) measurements are discussed in [25].

Orbit determination with measurements provided by a constellation of satellites is considered in [26] and [27]. The tracking and data relay satellite system (TDRSS) uses satellites in geostationary orbits to track satellites in low-Earth orbit (LEO), while the global positioning system (GPS) uses a constellation of satellites with pseudorange measurements, that is, range measurements with clock differentials, to determine the location of the user.

In this article we illustrate and compare SDEKF and SDUKF by considering a constellation of six spacecraft in circular LEO that tracks a satellite in geosynchronous orbit. Unlike the GPS configuration, we assume that all six satellites are in equatorial orbits. This assumption renders the estimation problem more difficult due to loss of observability as the target satellite leaves its equatorial orbit due to a change-in-inclination maneuver. Although inclining the orbits of the observing satellites makes the problem easier—and thus is the logical choice in practice—we consider the equatorial case because of the challenge it poses to nonlinear estimation algorithms. We also suspect, although we do not investigate this point, that unobservability can arise for alternative orbital configurations. If so, the deliberate choice of equatorial orbits provides a transparent case in which unobservability arises. In any event, the principles and methods discussed in this article can readily be applied to alternative configurations of the target and spacecraft.

Since the observing spacecraft have much shorter periods than the target satellite, we must account for blockage by the Earth, and thus the number of available measurements varies with time. We are particularly interested in the ability of the observing spacecraft to acquire and track

the target satellite with sparse measurements, that is, with a large sample interval. This objective is motivated by the need for satellites to simultaneously track a large number of objects. We thus compare the performance of the estimators for a range of sample intervals.

We focus on three main problems. First, we investigate the ability of the constellation of observing satellites to acquire the target satellite under poor initial information. Next, we consider the ability to track the eccentricity of the target satellite's orbit when it remains in an equatorial orbit. Finally, we consider the ability of the filters to track the target satellite when it changes its inclination away from the equatorial plane. Numerical examples are given to analyze the performance of both filters for each problem.

EQUATIONS OF MOTION

We consider a single body, called the *target*, orbiting the Earth. We assume a uniform, spherical Earth. The position vector $\vec{r}$ of the target relative to the center of the Earth satisfies

$$\ddot{\vec{r}} = \frac{-\mu}{r^3}\vec{r} + \vec{w}, \tag{1}$$

where $r \triangleq |\vec{r}|$ is the distance from the target to the center of the Earth, $\vec{w}$ denotes perturbing forces, such as thrusting, drag, and solar pressure, per unit mass acting on the target, $\mu \triangleq 398,600\ \text{km}^3/s^2$ is the Earth's gravitational parameter, and (ignoring forces applied to Earth) the frame derivatives are taken with respect to an arbitrary inertial frame I. Introducing the velocity vector $\vec{v} \triangleq \dot{\vec{r}}$, we can rewrite (1) as

$$\dot{\vec{r}} = \vec{v}, \tag{2}$$

$$\dot{\vec{v}} = \frac{-\mu}{r^3}\vec{r} + \vec{w}. \tag{3}$$

It is traditional to choose the inertial reference frame I so that the X-axis points toward the Sun on the first day of spring (the vernal equinox line), the Z-axis points through the geographic North pole of the Earth along its axis of rotation, and the Y-axis completes a right-handed coordinate system. The location of the origin of I is irrelevant [28] but is traditionally taken to be the center of the Sun. This description is approximate since the Earth's rotational axis is not fixed inertially [29, pp. 150–153]. However, such details play no role in the subsequent analysis.

Resolving $\vec{r}$, $\vec{v}$, and $\vec{w}$ in I according to

$$\vec{r}_{\text{I}} = \begin{bmatrix} x \\ y \\ z \end{bmatrix}, \quad \vec{v}_{\text{I}} = \begin{bmatrix} v_x \\ v_y \\ v_z \end{bmatrix}, \quad \vec{w}_{\text{I}} = \begin{bmatrix} w_x \\ w_y \\ w_z \end{bmatrix},$$

the equations of motion (2) and (3) become

$$\begin{bmatrix} \dot{x} \\ \dot{y} \\ \dot{z} \\ \dot{v}_x \\ \dot{v}_y \\ \dot{v}_z \end{bmatrix} = \begin{bmatrix} v_x \\ v_y \\ v_z \\ -(\mu/r^3)x + w_x \\ -(\mu/r^3)y + w_y \\ -(\mu/r^3)z + w_z \end{bmatrix}, \tag{4}$$

where $r \triangleq \sqrt{x^2 + y^2 + z^2}$. We can rewrite (4) as

$$\dot{X}(t) = f(X(t)) + W(t), \tag{5}$$

where (omitting the argument t on the right-hand side)

$$X(t) \triangleq \begin{bmatrix} x \\ y \\ z \\ v_x \\ v_y \\ v_z \end{bmatrix}, \quad f(X(t)) \triangleq \begin{bmatrix} v_x \\ v_y \\ v_z \\ -(\mu/r^3)x \\ -(\mu/r^3)y \\ -(\mu/r^3)z \end{bmatrix},$$

$$W(t) \triangleq \begin{bmatrix} 0 \\ 0 \\ 0 \\ w_x \\ w_y \\ w_z \end{bmatrix}. \tag{6}$$

The vector $X = X(t) \in \mathbb{R}^6$ provides a complete representation of the target's state, which is characterized by its position and velocity. When the satellite is moving along an orbit, such as a circle, ellipse, parabola, or hyperbola, it is often useful to represent the satellite motion in terms of the six orbital parameters given by the specific angular momentum h_{a}, the inclination i, the right ascension of the ascending node Ω, the eccentricity e, the argument of perigee ω, and the true anomaly $\nu(t)$. The angles Ω, i, and ω comprise a $(3, 1, 3)$ sequence of Euler rotations that transform the inertial frame I to the orbital frame. The angular momentum h_{a} and eccentricity e specify the size and shape of the orbit, while the true anomaly $\nu(t)$ is a time-dependent parameter that represents the position of the satellite along its orbit. The nonlinear transformations that convert position and velocity into orbital elements are given in "Orbital Elements."

MEASUREMENT MODELS

We consider the case in which satellites in LEO are observing a target satellite in a geostationary orbit. We assume that the LEO satellites are spaced uniformly around the Earth in circular equatorial orbits. All available satellite measurements are assumed to occur simultaneously at a fixed sample interval of size h.

Measurements from the ith satellite are unavailable when the line-of-sight path between the ith satellite and the target is blocked by the Earth. To determine blockage, we note that the Earth's surface blocks the path from the ith satellite, located at (x_i, y_i, z_i), to the target, located at (x, y, z), if and only if there exists $\alpha \in [0, 1]$ such that $D_i(\alpha) < R_E$, where $R_E \triangleq 6378$ km is the radius of the Earth and

$$D_i(\alpha) \triangleq \sqrt{[(1-\alpha)x_i+\alpha x]^2 + [(1-\alpha)y_i + \alpha y]^2 + [(1-\alpha)z_i + \alpha z]^2}.$$

The smallest value of $D_i(\alpha)$ is attained for $\alpha = \alpha_i$, where

$$\alpha_i \triangleq -\frac{x_i(x-x_i) + y_i(y-y_i) + z_i(z-z_i)}{(x-x_i)^2 + (y-y_i)^2 + (z-z_i)^2}.$$

Orbital Elements

Here, we present a method for calculating the six orbital elements $h_a, i, \Omega, e, \omega$, and ν from the target position $\vec{r}$ and velocity $\vec{v}$. Figure S1 illustrates the spacecraft orbit and orbital elements. The inertial reference frame I, defined in the main text, is denoted by unit vectors $\vec{I}, \vec{J}, \vec{K}$. First, we calculate the norm of the orbital distance $\vec{r}$, the norm of the orbital velocity $\vec{v}$, and the radial velocity v_r by means of

$$r \triangleq \sqrt{\vec{r}\cdot\vec{r}}, \tag{S1}$$
$$v \triangleq \sqrt{\vec{v}\cdot\vec{v}}, \tag{S2}$$
$$v_r \triangleq \frac{\vec{r}\cdot\vec{v}}{r}. \tag{S3}$$

Note that $v_r > 0$ indicates that the target is moving away from perigee.

The *specific angular momentum* $\vec{h}_a$ lies normal to the orbital plane and is obtained by

$$\vec{h}_a \triangleq \vec{r} \times \vec{v}, \tag{S4}$$
$$h_a \triangleq \sqrt{\vec{h}_a \cdot \vec{h}_a}. \tag{S5}$$

Inclination i is the angle between the equatorial plane and the orbital plane. Equivalently, inclination is the angle between the inertial Z-axis and $\vec{h}_a$, which is normal to the orbital plane, so that

$$i \triangleq \cos^{-1}\left(\frac{\vec{h}_a \cdot \vec{K}}{h_a}\right) \tag{S6}$$

Next, we calculate the node line $\vec{N}$ and its magnitude N by

$$\vec{N} \triangleq \vec{K} \times \vec{h}_a, \tag{S7}$$
$$N \triangleq \sqrt{\vec{N}\cdot\vec{N}}, \tag{S8}$$

which locate the point at which the target's orbit ascends from the equatorial plane. The *right ascension of the ascending node*

$$\Omega \triangleq \cos^{-1}\left(\frac{\vec{N}\cdot\vec{I}}{N}\right) \tag{S9}$$

represents the angle between the inertial X-axis and the node line $\vec{N}$. Note that, if $\vec{N}\cdot\vec{J} \geq 0$, then $0^\circ \leq \Omega < 180^\circ$ whereas, if $\vec{N}\cdot\vec{J} < 0$, then $180^\circ \leq \Omega < 360^\circ$.

The *eccentricity* vector $\vec{e}$, which points toward the target orbit's perigee, is obtained by

$$\vec{e} \triangleq \frac{1}{\mu}\left[\left(\frac{v^2-\mu}{r}\right)\vec{r} - r v_r \vec{v}\right], \tag{S10}$$
$$e \triangleq \sqrt{\vec{e}\cdot\vec{e}}. \tag{S11}$$

The *argument of perigee* ω denotes the angle between the node line and the eccentricity vector, that is,

$$\omega \triangleq \cos^{-1}\left(\frac{\vec{N}\cdot\vec{e}}{Ne}\right). \tag{S12}$$

Note that, if $\vec{e}\cdot\vec{K} \geq 0$, then $0^\circ \leq \omega < 180^\circ$, whereas, if $\vec{e}\cdot\vec{K} < 0$, then $180^\circ \leq \omega < 360^\circ$. Finally, the *true anomaly* ν, which represents the angle between the eccentricity vector and the target's position vector, is calculated by

$$\nu = \cos^{-1}\left(\frac{\vec{e}\cdot\vec{r}}{er}\right). \tag{S13}$$

Note that, if $v_r \geq 0$, then $0^\circ \leq \nu < 180^\circ$ whereas, if $v_r < 0$, then $180^\circ \leq \nu < 360^\circ$.

These nonlinear transformations along with a Matlab routine are given in [29].

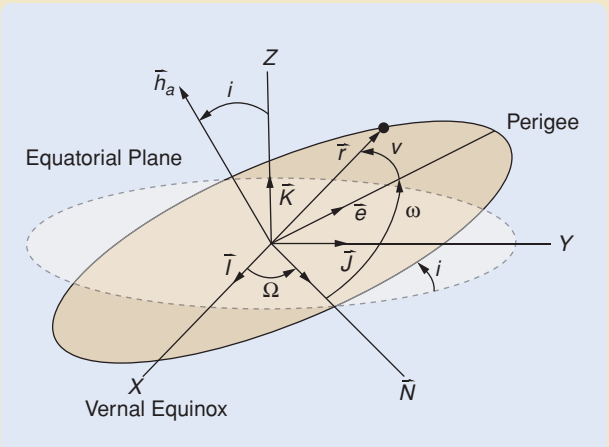

FIGURE S1 Orbit orientation with respect to the geocentric-equatorial frame. The six orbital elements are the specific angular momentum h_a, inclination i, right ascension of the ascending node Ω, eccentricity e, argument of perigee ω, and true anomaly ν.

Hence, we compute α_i, determine whether α_i lies in the interval $[0, 1]$, and then check the blockage condition $D_i(\alpha_i) < R_E$.

Range-Only Measurements

For range-only trajectory estimation, we assume that range measurements are available from p_k satellites at times $t = kh$, where $k = 1, 2, \ldots$. Note that the number p_k of satellites observing the target at time kh is a function of k due to blockage by the Earth. The measurement $Y = Y(kh) \in \mathbb{R}^{p_k}$ is given by (omitting the argument kh on the right-hand side)

$$Y(kh) = \begin{bmatrix} d_1(x, y, z, x_1, y_1, z_1) \\ \vdots \\ d_{p_k}(x, y, z, x_{p_k}, y_{p_k}, z_{p_k}) \end{bmatrix} + V_d(kh), \qquad (7)$$

where, for $i = 1, \ldots, p_k$,

$$d_i(x, y, z, x_i, y_i, z_i) \triangleq [(x - x_i)^2 + (y - y_i)^2 + (z - z_i)^2]^{1/2} \qquad (8)$$

is the distance from the ith satellite to the target, and $V_d(kh) \in \mathbb{R}^{p_k}$ denotes range-measurement noise.

Range and Angle Measurements

We now assume that azimuth- and elevation-angle data are used in conjunction with range data. Azimuth refers to the counterclockwise angle from the inertial X-axis to the target projected onto the inertial XY-plane, while elevation refers to the angle (positive above the XY-plane) from the projection of the target onto the inertial XY-plane to the target. The measurement $Y = Y(kh) \in \mathbb{R}^{3p_k}$ is given by (again omitting the argument kh)

$$Y(kh) = \begin{bmatrix} d_1(x, y, z, x_1, y_1, z_1) \\ \vdots \\ d_{p_k}(x, y, z, x_{p_k}, y_{p_k}, z_{p_k}) \\ A_1(x, y, z, x_1, y_1, z_1) \\ \vdots \\ A_{p_k}(x, y, z, x_{p_k}, y_{p_k}, z_{p_k}) \\ E_1(x, y, z, x_1, y_1, z_1) \\ \vdots \\ E_{p_k}(x, y, z, x_{p_k}, y_{p_k}, z_{p_k}) \end{bmatrix} + \begin{bmatrix} V_d(kh) \\ V_\theta(kh) \end{bmatrix}, \qquad (9)$$

where, for $i = 1, \ldots, p_k$, with $\jmath = \sqrt{-1}$,

$$A_i(x, y, z, x_i, y_i, z_i) \triangleq \angle(x - x_i + \jmath(y - y_i)), \qquad (10)$$

$$E_i(x, y, z, x_i, y_i, z_i) \triangleq \angle\left(\sqrt{(x - x_i)^2 + (y - y_i)^2} + \jmath(z - z_i)\right), \qquad (11)$$

are the azimuth and elevation angles, respectively, from the ith satellite to the target, and $V_\theta(kh) \in \mathbb{R}^{2p_k}$ is the angle-measurement noise.

Range-rate measurements can be used to further augment the available measurements. For $i = 1, \ldots, p_k$,

$$\dot{d}_i(x, y, z, x_i, y_i, z_i, \dot{x}, \dot{y}, \dot{z}, \dot{x}_i, \dot{y}_i, \dot{z}_i) \triangleq \frac{(x - x_i)(\dot{x} - \dot{x}_i) + (y - y_i)(\dot{y} - \dot{y}_i) + (z - z_i)(\dot{z} - \dot{z}_i)}{d_i(x, y, z, x_i, y_i, z_i)}$$

is the range-rate measurement from the ith satellite to the target. Simulations (not included) that incorporate range-rate measurements show little estimation improvement over the use of range and angle measurements alone. Hence, range-rate measurements are not considered further.

For generality, we write the measurement map given by (7) for range-only data and given by (9) for range and angle data as

$$Y(kh) = g(X(kh)) + V(kh), \qquad (12)$$

where $V(kh) = V_d(kh)$ for range-only data and

$$V(kh) = \begin{bmatrix} V_d(kh) \\ V_\theta(kh) \end{bmatrix}$$

for range and angle data.

FORECAST AND DATA-ASSIMILATION STEPS

SDEKF and SDUKF are two-step estimators. In the *forecast step*, model information is used during the interval $[(k-1)h, kh]$, while, in the *data-assimilation step*, a data update is performed at each time $t = kh$. We denote the forecast state estimate $\hat{X}^{\mathrm{f}}(t)$ by

$$\hat{X}^{\mathrm{f}}(t) \triangleq \begin{bmatrix} \hat{x}^{\mathrm{f}} & \hat{y}^{\mathrm{f}} & \hat{z}^{\mathrm{f}} & \hat{v}_x^{\mathrm{f}} & \hat{v}_y^{\mathrm{f}} & \hat{v}_z^{\mathrm{f}} \end{bmatrix}^{\mathrm{T}}$$

and the forecast error covariance $P_0^{\mathrm{f}}(t)$ by

$$P_0^{\mathrm{f}}(t) \triangleq \mathcal{E}\left[(X(t) - \hat{X}^{\mathrm{f}}(t))(X(t) - \hat{X}^{\mathrm{f}}(t))^{\mathrm{T}}\right]$$

before data updates. After data updates, the data-assimilation state estimate $\hat{X}^{\mathrm{da}}(kh)$ is given by

$$\hat{X}^{\mathrm{da}}(kh) \triangleq \begin{bmatrix} \hat{x}^{\mathrm{da}} & \hat{y}^{\mathrm{da}} & \hat{z}^{\mathrm{da}} & \hat{v}_x^{\mathrm{da}} & \hat{v}_y^{\mathrm{da}} & \hat{v}_z^{\mathrm{da}} \end{bmatrix}^{\mathrm{T}},$$

while the data-assimilation error covariance $P_0^{\mathrm{da}}(kh)$ is given by

$$P_0^{\mathrm{da}}(kh) \triangleq \mathcal{E}[(X(kh) - \hat{X}^{\mathrm{da}}(kh))(X(kh) - \hat{X}^{\mathrm{da}}(kh))^{\mathrm{T}}].$$

In the following sections, we present the SDEKF and SDUKF filters. Since these filters are approximate, we cannot propagate the true forecast and data-assimilation error covariances $P_0^{\mathrm{f}}(t)$ and $P_0^{\mathrm{da}}(kh)$. Rather, we propagate the pseudo forecast-error covariance $P^{\mathrm{f}}(t)$ and the pseudo

data-assimilation error covariance $P^{\mathrm{da}}(kh)$. Let $\hat{X}^{\mathrm{da}}(0)$ and $P^{\mathrm{da}}(0)$ denote the initial state estimate and the initial error covariance, respectively. $P^{\mathrm{da}}(0)$ accounts for uncertainty in the initial estimate.

SAMPLED-DATA EXTENDED KALMAN FILTER

In this section we summarize the equations for SDEKF. For details, see [1] and [2].

Forecast Step

The forecast (data-free) step of SDEKF consists of the state-estimate propagation

$$\dot{\hat{X}}^{\mathrm{f}}(t) = f(\hat{X}^{\mathrm{f}}(t)), \quad t \in [(k-1)h, kh], \tag{13}$$

as well as the forecast pseudo-error covariance propagation

$$\dot{P}^{\mathrm{f}}(t) = \hat{A}(t)P^{\mathrm{f}}(t) + P^{\mathrm{f}}(t)\hat{A}^{\mathrm{T}}(t) + Q, \quad t \in [(k-1)h, kh], \tag{14}$$

where

$$\hat{A}(t) \triangleq \left.\frac{\partial f(X(t))}{\partial t}\right|_{X(t)=\hat{X}^{\mathrm{f}}(t)}$$

is the Jacobian of f evaluated along the trajectory of (13). In the traditional linear setting, Q represents the state noise covariance, while, in the orbit-estimation problem, Q accounts for unmodeled effects such as perturbing forces. The Jacobian $\hat{A}(t)$ is given by

$$\hat{A}(t) \triangleq \begin{bmatrix} 0_{3\times 3} & I_3 \\ \hat{A}_0(t) & 0_{3\times 3} \end{bmatrix},$$

where (omitting the argument t)

$$A_0(t) \triangleq \mu \begin{bmatrix} \frac{3(\hat{x}^{\mathrm{f}})^2}{(\hat{r}^{\mathrm{f}})^5} - \frac{1}{(\hat{r}^{\mathrm{f}})^3} & \frac{3\hat{x}^{\mathrm{f}}\hat{y}^{\mathrm{f}}}{(\hat{r}^{\mathrm{f}})^5} & \frac{3\hat{x}^{\mathrm{f}}\hat{z}^{\mathrm{f}}}{(\hat{r}^{\mathrm{f}})^5} \\ \frac{3\hat{x}^{\mathrm{f}}\hat{y}^{\mathrm{f}}}{(\hat{r}^{\mathrm{f}})^5} & \frac{3(\hat{y}^{\mathrm{f}})^2}{(\hat{r}^{\mathrm{f}})^5} - \frac{1}{(\hat{r}^{\mathrm{f}})^3} & \frac{3\hat{y}^{\mathrm{f}}\hat{z}^{\mathrm{f}}}{(\hat{r}^{\mathrm{f}})^5} \\ \frac{3\hat{x}^{\mathrm{f}}\hat{z}^{\mathrm{f}}}{(\hat{r}^{\mathrm{f}})^5} & \frac{3\hat{y}^{\mathrm{f}}\hat{z}^{\mathrm{f}}}{(\hat{r}^{\mathrm{f}})^5} & \frac{3(\hat{z}^{\mathrm{f}})^2}{(\hat{r}^{\mathrm{f}})^5} - \frac{1}{(\hat{r}^{\mathrm{f}})^3} \end{bmatrix},$$

where $\hat{r}^{\mathrm{f}} \triangleq \sqrt{(\hat{x}^{\mathrm{f}})^2 + (\hat{y}^{\mathrm{f}})^2 + (\hat{z}^{\mathrm{f}})^2}$.

A timing diagram illustrating the sequence of calculations is shown in Figure 1. Equations (13) and (14) are numerically integrated online from $(k-1)h$ to kh with initial values obtained from the data-assimilation step described below, that is, $\hat{X}^{\mathrm{f}}((k-1)h) = \hat{X}^{\mathrm{da}}((k-1)h)$ and $P^{\mathrm{f}}((k-1)h) = P^{\mathrm{da}}((k-1)h)$. Since no data injection occurs during the time interval $[(k-1)h, kh]$, variable-step-size integration with specified tolerance is used for efficiency and accuracy as long as the integration of (13) and (14) is completed before time kh occurs. Let $\hat{X}^{\mathrm{f}}(kh)$ and $P^{\mathrm{f}}(kh)$ denote the values of $\hat{X}^{\mathrm{f}}$ and P^{f} at the right-hand endpoint of the interval $[(k-1)h, kh]$. The overall system can be viewed as a sampled-data system in which continuous-time dynamics are interrupted by instantaneous state jumps [30].

Data-Assimilation Step

Let $x_i(kh), y_i(kh), z_i(kh)$ denote the inertial-frame coordinates of the ith satellite at time kh, assumed to be known accurately. For the data-assimilation step, the linearized measurement map

$$\hat{C}(k) \triangleq \left.\frac{\partial g(X(kh))}{\partial k}\right|_{X(kh)=\hat{X}^{\mathrm{f}}(kh)}$$

for range-only data is given by

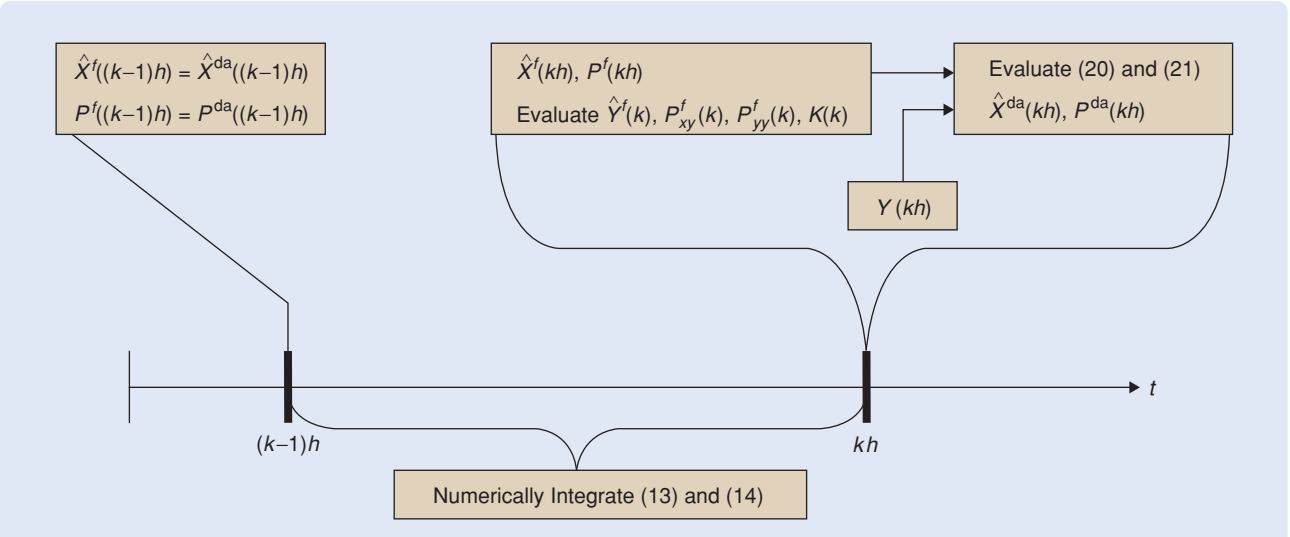

FIGURE 1 Timing diagram for the sampled-data extended Kalman filter. The forecast and data-assimilation steps are assumed to occur in zero time at time $t = kh$.

$$\hat{C}(k) \triangleq \begin{bmatrix} \frac{\tilde{x}_1^{\mathrm{f}}(k)}{\hat{d}_1^{\mathrm{f}}(k)} & \frac{\tilde{y}_1^{\mathrm{f}}(k)}{\hat{d}_1^{\mathrm{f}}(k)} & \frac{\tilde{z}_1^{\mathrm{f}}(k)}{\hat{d}_1^{\mathrm{f}}(k)} & 0_{1\times 3} \\ \vdots & \vdots & \vdots & \vdots \\ \frac{\tilde{x}_{p_k}^{\mathrm{f}}(k)}{\hat{d}_{p_k}^{\mathrm{f}}(k)} & \frac{\tilde{y}_{p_k}^{\mathrm{f}}(k)}{\hat{d}_{p_k}^{\mathrm{f}}(k)} & \frac{\tilde{z}_{p_k}^{\mathrm{f}}(k)}{\hat{d}_{p_k}^{\mathrm{f}}(k)} & 0_{1\times 3} \end{bmatrix}, \tag{15}$$

where, for $i = 1, \ldots, p_k$,

$$\begin{aligned} \tilde{x}_i^{\mathrm{f}}(k) &\triangleq \hat{x}^{\mathrm{f}}(kh) - x_i(kh), \\ \tilde{y}_i^{\mathrm{f}}(k) &\triangleq \hat{y}^{\mathrm{f}}(kh) - y_i(kh), \\ \tilde{z}_i^{\mathrm{f}}(k) &\triangleq \hat{z}^{\mathrm{f}}(kh) - z_i(kh), \\ \hat{d}_i^{\mathrm{f}}(k) &\triangleq d_i(\hat{x}^{\mathrm{f}}(kh), \hat{y}^{\mathrm{f}}(kh), \hat{z}^{\mathrm{f}}(kh), x_i(kh), y_i(kh), z_i(kh)), \end{aligned}$$

and $d_i(\cdot)$ is defined by (8). For range and angle data, the linearized measurement map is given by

$$\hat{C}(k) \triangleq \begin{bmatrix} \frac{\tilde{x}_1^{\mathrm{f}}(k)}{\hat{d}_1^{\mathrm{f}}(k)} & \frac{\tilde{y}_1^{\mathrm{f}}(k)}{\hat{d}_1^{\mathrm{f}}(k)} & \frac{\tilde{z}_1^{\mathrm{f}}(k)}{\hat{d}_1^{\mathrm{f}}(k)} & 0_{1\times 3} \\ \vdots & \vdots & \vdots & \vdots \\ \frac{\tilde{x}_{p_k}^{\mathrm{f}}(k)}{\hat{d}_{p_k}^{\mathrm{f}}(k)} & \frac{\tilde{y}_{p_k}^{\mathrm{f}}(k)}{\hat{d}_{p_k}^{\mathrm{f}}(k)} & \frac{\tilde{z}_{p_k}^{\mathrm{f}}(k)}{\hat{d}_{p_k}^{\mathrm{f}}(k)} & 0_{1\times 3} \\ -\frac{\tilde{y}_1^{\mathrm{f}}(k)}{(\hat{\delta}_1^{\mathrm{f}}(k))^2} & \frac{\tilde{x}_1^{\mathrm{f}}(k)}{(\hat{\delta}_1^{\mathrm{f}}(k))^2} & 0 & 0_{1\times 3} \\ \vdots & \vdots & \vdots & \vdots \\ -\frac{\tilde{y}_{p_k}^{\mathrm{f}}(k)}{(\hat{\delta}_{p_k}^{\mathrm{f}}(k))^2} & \frac{\tilde{x}_{p_k}^{\mathrm{f}}(k)}{(\hat{\delta}_{p_k}^{\mathrm{f}}(k))^2} & 0 & 0_{1\times 3} \\ -\frac{\tilde{x}_1^{\mathrm{f}}(k)\tilde{z}_1^{\mathrm{f}}(k)}{\hat{\delta}_1^{\mathrm{f}}(k)(\hat{d}_1^{\mathrm{f}}(k))^2} & -\frac{\tilde{y}_1^{\mathrm{f}}(k)\tilde{z}_1^{\mathrm{f}}(k)}{\hat{\delta}_1^{\mathrm{f}}(k)(\hat{d}_1^{\mathrm{f}}(k))^2} & \frac{\hat{\delta}_1^{\mathrm{f}}(k)}{(\hat{d}_1^{\mathrm{f}}(k))^2} & 0_{1\times 3} \\ \vdots & \vdots & \vdots & \vdots \\ -\frac{\tilde{x}_{p_k}^{\mathrm{f}}(k)\tilde{z}_{p_k}^{\mathrm{f}}(k)}{\hat{\delta}_{p_k}^{\mathrm{f}}(k)(\hat{d}_{p_k}^{\mathrm{f}}(k))^2} & -\frac{\tilde{y}_{p_k}^{\mathrm{f}}(k)\tilde{z}_{p_k}^{\mathrm{f}}(k)}{\hat{\delta}_{p_k}^{\mathrm{f}}(k)(\hat{d}_{p_k}^{\mathrm{f}}(k))^2} & \frac{\hat{\delta}_{p_k}^{\mathrm{f}}(k)}{(\hat{d}_{p_k}^{\mathrm{f}}(k))^2} & 0_{1\times 3} \end{bmatrix} \tag{16}$$

where, for $i = 1, \ldots, p_k$,

$$\hat{\delta}_i^{\mathrm{f}}(k) \triangleq \sqrt{\left(\tilde{x}_i^{\mathrm{f}}(k)\right)^2 + \left(\tilde{y}_i^{\mathrm{f}}(k)\right)^2}.$$

Furthermore, the data-assimilation gain $K(k)$ is given by

$$K(k) = P_{xy}^{\mathrm{f}}(k)[P_{yy}^{\mathrm{f}}(k)]^{-1}, \tag{17}$$

where the pseudo forecast cross covariance and pseudo forecast innovation covariance are, respectively, given by

$$P_{xy}^{\mathrm{f}}(k) = P^{\mathrm{f}}(kh)\hat{C}^{\mathrm{T}}(k), \tag{18}$$

$$P_{yy}^{\mathrm{f}}(k) = \hat{C}(k)P^{\mathrm{f}}(kh)\hat{C}^{\mathrm{T}}(k) + R, \tag{19}$$

where R is the covariance of the measurement noise $V(kh)$. The data-assimilation state estimate is given by

$$X^{\mathrm{da}}(kh) = \hat{X}^{\mathrm{f}}(kh) + K(k)[Y(kh) - \hat{Y}^{\mathrm{f}}(k)], \tag{20}$$

$$P^{\mathrm{da}}(kh) = P^{\mathrm{f}}(kh) - K(k)P_{yy}^{\mathrm{f}}(k)K^{\mathrm{T}}(k), \tag{21}$$

where, for range-only data,

$$\hat{Y}^{\mathrm{f}}(k) \triangleq \begin{bmatrix} \hat{d}_1^{\mathrm{f}}(k) \cdots \hat{d}_{p_k}^{\mathrm{f}}(k) \end{bmatrix}^{\mathrm{T}} \tag{22}$$

and, for range and angle data,

$$\hat{Y}^{\mathrm{f}}(k) \triangleq \begin{bmatrix} \hat{d}_1^{\mathrm{f}}(k) \cdots \hat{d}_{p_k}^{\mathrm{f}}(k) & \hat{A}_1^{\mathrm{f}}(k) \cdots \hat{A}_{p_k}^{\mathrm{f}}(k) & \hat{E}_1^{\mathrm{f}}(k) \cdots \hat{E}_{p_k}^{\mathrm{f}}(k) \end{bmatrix}^{\mathrm{T}}, \tag{23}$$

where, for $i = 1, \ldots, p_k$,

$$\begin{aligned} \hat{A}_i^{\mathrm{f}}(k) &\triangleq A_i(\hat{x}^{\mathrm{f}}(kh), \hat{y}^{\mathrm{f}}(kh), \hat{z}^{\mathrm{f}}(kh), x_i(kh), y_i(kh), z_i(kh)), \\ \hat{E}_i^{\mathrm{f}}(k) &\triangleq E_i(\hat{x}^{\mathrm{f}}(kh), \hat{y}^{\mathrm{f}}(kh), \hat{z}^{\mathrm{f}}(kh), x_i(kh), y_i(kh), z_i(kh)), \end{aligned}$$

where $A_i(\cdot)$ and $E_i(\cdot)$ are defined by (10) and (11). The values $\hat{X}^{\mathrm{da}}(kh)$ and $P^{\mathrm{da}}(kh)$ are used to initialize (13) and (14) in the next interval $[kh, (k+1)h]$.

UNSCENTED KALMAN FILTER

An alternative approach to state estimation for an nth-order nonlinear system is UKF [14]. Unlike EKF, UKF does not rely on linearization of the dynamical equations and measurement map. Instead, UKF uses the unscented transform (UT) [15], which is a numerical procedure for approximating the posterior mean and covariance of a random vector obtained from a nonlinear transformation.

Let X denote a random vector whose mean $\bar{X} \in \mathbb{R}^n$ and covariance $\bar{P} \in \mathbb{R}^{n\times n}$ are assumed to be known. Also, let Y be a random vector with mean $\bar{Y} \in \mathbb{R}^p$ and covariance $\bar{P}_{yy} \in \mathbb{R}^{p\times p}$ obtained from the nonlinear transformation $Y = g(X)$. The application of UT to estimate $\bar{Y}$ and $\bar{P}_{yy}$ begins with a set of deterministically chosen sample vectors $\mathcal{X}_j \in \mathbb{R}^n$, $j = 0, \ldots, 2n$, known as sigma points. To satisfy

$$\sum_{j=0}^{2n} \gamma_{x,j}\mathcal{X}_j = \bar{X}$$

and

$$\sum_{j=0}^{2n} \gamma_{P,j}(\mathcal{X}_j - \bar{X})(\mathcal{X}_j - \bar{X})^{\mathrm{T}} = \bar{P},$$

the sigma-point matrix given by $\mathcal{X} \triangleq [\mathcal{X}_0\ \mathcal{X}_1\ \ldots\ \mathcal{X}_{2n}] \in \mathbb{R}^{n\times(2n+1)}$ is chosen as

$$\mathcal{X} \triangleq \bar{X}1_{1\times(2n+1)} + \sqrt{n+\lambda}\,[\,0_{n\times 1} \quad P_{\mathrm{Ch}} \quad -P_{\mathrm{Ch}}\,],$$

with weights

$$\gamma_{x,0} \triangleq \frac{\lambda}{n+\lambda}, \quad \gamma_{P,0} \triangleq \frac{\lambda}{n+\lambda} + (1-\alpha^2+\beta),$$
$$\gamma_{x,j} = \gamma_{P,j} \triangleq \frac{1}{2(n+\lambda)}, \quad j = 1, \ldots, 2n,$$

where $P_{\mathrm{Ch}} \in \mathbb{R}^{n\times n}$ is the lower triangular Cholesky square root satisfying

$$P_{\mathrm{Ch}} P_{\mathrm{Ch}}^{\mathrm{T}} = \bar{P},$$

$0 < \alpha \leq 1$, $\beta > 0$, $\kappa > 0$, and $\lambda \triangleq \alpha^2(n+\kappa) - n > -n$ determines the spread of the sigma points around $\bar{X}$. In practice, α, β, and κ are chosen by numerical experience to improve filter convergence [15]. Propagating each sigma point through g yields

$$\mathcal{Y}_j = g(\mathcal{X}_j), \quad j = 0, \ldots, 2n,$$

such that

$$\bar{Y} = \sum_{j=0}^{2n} \gamma_{x,j} \mathcal{Y}_j,$$
$$\bar{P}_{yy} = \sum_{j=0}^{2n} \gamma_{P,j} [\mathcal{Y}_j - \bar{Y}][\mathcal{Y}_j - \bar{Y}]^{\mathrm{T}}.$$

UT yields the true mean $\bar{Y}$ and true covariance $\bar{P}_{yy}$ if $g = g_1 + g_2$, where g_1 is linear and g_2 is quadratic [15]. Otherwise, $\bar{Y}$ is a *pseudo mean*, and $\bar{P}_{yy}$ is a *pseudo covariance*.

SAMPLED-DATA UNSCENTED KALMAN FILTER

In this section we present the equations for SDUKF developed in [16]. As in the case of SDEKF, the procedure consists of a forecast step and a data assimilation step. These equations are presented for the case $n = 6$ in accordance with the satellite equations of motion (5) and (6).

Forecast Step

The forecast step of SDUKF consists of the sigma-point propagation

$$\mathcal{X}(t) = \hat{X}^{\mathrm{f}}(t) 1_{1\times 13} + \sqrt{\lambda+6}\,[\,0_{6\times 1} \quad P^{\mathrm{f}}_{\mathrm{Ch}}(t) \quad -P^{\mathrm{f}}_{\mathrm{Ch}}(t)\,], \quad t \in [(k-1)h, kh], \tag{24}$$

$$\dot{\hat{X}}^{\mathrm{f}}(t) \triangleq \sum_{j=0}^{12} \gamma_{x,j} f(\mathcal{X}_j(t)), \quad t \in [(k-1)h, kh], \tag{25}$$

as well as the pseudo error covariance propagation

$$\dot{P}^{\mathrm{f}}(t) = \sum_{j=0}^{12} \gamma_{P,j} [\mathcal{X}_j(t) - \hat{X}^{\mathrm{f}}(t)][f(\mathcal{X}_j(t)) - \dot{\hat{X}}^{\mathrm{f}}(t)]^{\mathrm{T}} + \sum_{j=0}^{12} \gamma_{P,j} [f(\mathcal{X}_j(t)) - \dot{\hat{X}}^{\mathrm{f}}(t)][\mathcal{X}_j(t) - \hat{X}^{\mathrm{f}}(t)]^{\mathrm{T}} + Q, \quad t \in [(k-1)h, kh]. \tag{26}$$

A timing diagram illustrating the sequence of calculations of SDUKF is shown in Figure 2. Equations (25) and (26) are numerically integrated online with initial values $X^{\mathrm{f}}((k-1)h) = X^{\mathrm{da}}((k-1)h)$ and $P^{\mathrm{f}}((k-1)h) = P^{\mathrm{da}}((k-1)h)$ given by the data-assimilation step at time $(k-1)h$. Let $\hat{X}^{\mathrm{f}}(kh)$ and $P^{\mathrm{f}}(kh)$ denote, respectively, the values of $\hat{X}^{\mathrm{f}}$ and P^{f} at the right-hand endpoint of the interval $[(k-1)h, kh]$.

Data-Assimilation Step

The data update step is given by

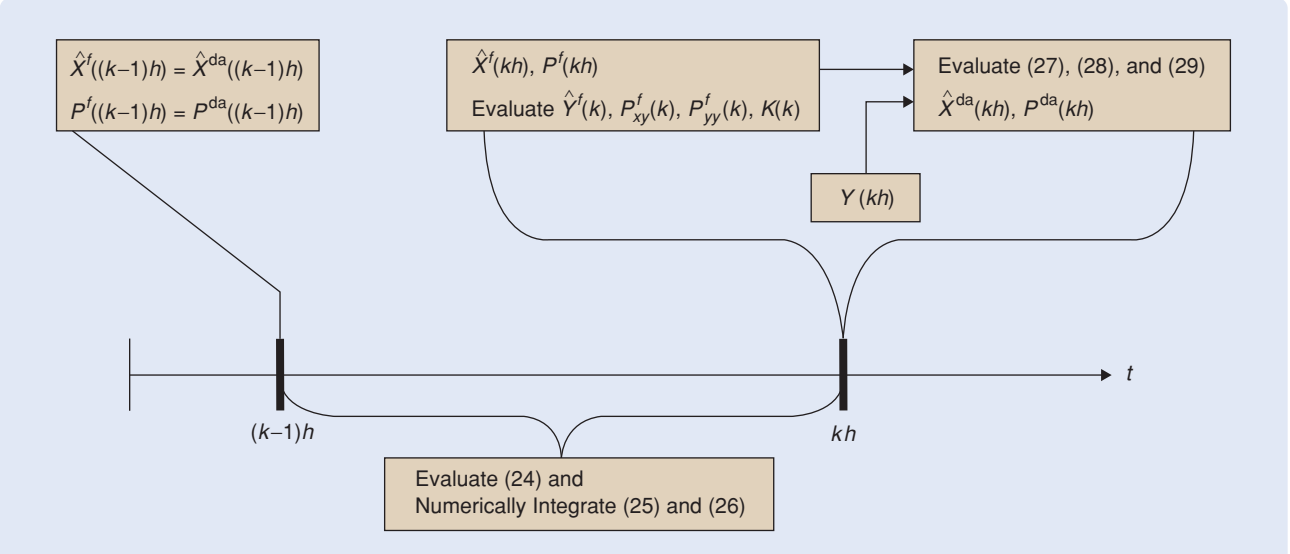

FIGURE 2 Timing diagram for the sampled-data unscented Kalman filter. The forecast and data-assimilation steps are assumed to occur in zero time at time $t = kh$.

$$\mathcal{X}(kh) = \hat{X}^{\mathrm{f}}(kh)1_{1\times 13} + \sqrt{\lambda+6} \times \left[\, 0_{6\times 1} \quad P^{\mathrm{f}}_{\mathrm{Ch}}(kh) \quad -P^{\mathrm{f}}_{\mathrm{Ch}}(kh) \,\right], \tag{27}$$

$$\hat{X}^{\mathrm{da}}(kh) = \hat{X}^{\mathrm{f}}(kh) + K(k)[Y(kh) - \hat{Y}^{\mathrm{f}}(k)], \tag{28}$$

$$P^{\mathrm{da}}(kh) = P^{\mathrm{f}}(kh) - K(k)P^{\mathrm{f}}_{yy}(k)K^{\mathrm{T}}(k), \tag{29}$$

where

$$K(k) = P^{\mathrm{f}}_{xy}(k)\left[P^{\mathrm{f}}_{yy}(k)\right]^{-1}, \tag{30}$$

$$\hat{Y}^{\mathrm{f}}(k) = \sum_{j=0}^{12} \gamma_{x,\,j}\,\mathcal{Y}_j(k), \tag{31}$$

$$P^{\mathrm{f}}_{xy}(k) = \sum_{j=0}^{12} \gamma_{P,\,j}[\mathcal{X}_j(kh) - \hat{X}^{\mathrm{f}}(kh)][\mathcal{Y}_j(k) - \hat{Y}^{\mathrm{f}}(k)]^{\mathrm{T}}, \tag{32}$$

$$P^{\mathrm{f}}_{yy}(k) = \sum_{j=0}^{12} \gamma_{P,\,j}[\mathcal{Y}_j(k) - \hat{Y}^{\mathrm{f}}(k)][\mathcal{Y}_j(k) - \hat{Y}^{\mathrm{f}}(k)]^{\mathrm{T}} + R. \tag{33}$$

For $j = 0, \ldots, 12$, $\mathcal{Y}_j(k)$ is given for range measurements by

$$\mathcal{Y}_j(k) \triangleq [\,\mathcal{D}_1(k) \quad \cdots \quad \mathcal{D}_{p_k}(k)\,]^{\mathrm{T}}, \tag{34}$$

where, for $i = 1, \ldots, p_k$,

$$\mathcal{D}_i(k) \triangleq d_i(\mathcal{X}_{i,1}(kh), \mathcal{X}_{i,2}(kh), \mathcal{X}_{i,3}(kh), x_i(kh), y_i, (kh)z_i(kh))$$

and $d_i(\cdot)$ is defined in (8). Alternatively, for range and angle measurements, $\mathcal{Y}_j(k)$ is given by (35), shown at the bottom of the page, where, for $i = 1, \ldots, p_k$,

$$\mathcal{A}_i(k) \triangleq A_i(\mathcal{X}_{i,1}(kh), \mathcal{X}_{i,2}(kh), \mathcal{X}_{i,3}(kh), x_i(kh), y_i(kh), z_i(kh)),$$
$$\mathcal{E}_i(k) \triangleq E_i(\mathcal{X}_{i,1}(kh), \mathcal{X}_{i,2}(kh), \mathcal{X}_{i,3}(kh), x_i(kh), y_i(kh), z_i(kh)),$$

and $A_i(\cdot)$ and $E_i(\cdot)$ are defined in (10) and (11), respectively. The values $\hat{X}^{\mathrm{da}}(kh)$ and $P^{\mathrm{da}}(kh)$ are used to initialize (25) and (26) in the next interval $[kh, (k+1)h]$.

NUMERICAL EXAMPLES

We consider the case in which six satellites in circular LEO at a radius of 6600 km are observing a target satellite in an equatorial geosynchronous orbit at a radius of 42,164 km. The number six represents the smallest number of satellites for which at least three satellites are always able to view the target. In fact, with six satellites in circular LEO, p_k switches between three and four.

Assuming perfect knowledge of the target's initial condition and assuming that the target is not maneuvering and all perturbing forces such as drag and solar pressure are known, it is possible to predict the target's motion with arbitrary accuracy without using measurements. However, when either the initial state is unknown, the target is maneuvering, or perturbing forces are present, measurements are needed to track the target. We consider the first two cases using both SDEKF and SDUKF.

Performance Assessment

Since SDEKF and SDUKF provide suboptimal estimates of the spacecraft trajectory, we use four metrics to compare their performance over an m-run Monte Carlo simulation. Let $\hat{X}^{\mathrm{da}}_{i,j}(kh)$ denote the state estimate of $X_i(kh)$, $i = 1, \ldots, 6$, for the jth Monte Carlo simulation, where $j = 1, \ldots, m$.

First, the *accuracy* of the state estimates $\hat{X}^{\mathrm{da}}_{i,j}(kh)$ given by (20) and (28), respectively, over $[k_0, k_{\mathrm{f}}]$ and over m Monte Carlo simulations is quantified by the root mean square error (RMSE) index

$$\mathrm{RMSE}_i \triangleq \frac{1}{m}\sum_{j=1}^{m}\left[\sqrt{\frac{1}{k_{\mathrm{f}}-k_0+1}\sum_{k=k_0}^{k_{\mathrm{f}}}\left(X_i(kh) - \hat{X}^{\mathrm{da}}_{i,j}(kh)\right)^2}\right], \quad i = 1, \ldots, 6, \tag{36}$$

where $X_i(kh)$ is the true value of the state.

We measure how *biased* the state estimate $\hat{X}^{\mathrm{da}}_{i,j}(kh)$ is by evaluating the RMSE of the sample mean of the estimate error over $[k_0, k_{\mathrm{f}}]$ and over m Monte Carlo simulations, that is,

$$\mathrm{B}_i \triangleq \sqrt{\frac{1}{k_{\mathrm{f}}-k_0+1}\sum_{k=k_0}^{k_{\mathrm{f}}}\left[\frac{1}{m}\sum_{j=1}^{m}\left(X_i(kh) - \hat{X}^{\mathrm{da}}_{i,j}(kh)\right)\right]^2}, \quad i = 1, \ldots, 6. \tag{37}$$

Simulation results (not included) show that the indices RMSE_i and B_i are similar. Hence, B_i is not considered further. Note that, to calculate RMSE_i and B_i, $X(kh)$ must be known, and thus these indices are restricted to simulation studies and cannot be evaluated in practice.

Next, let $P^{\mathrm{da}}_j(kh)$ denote the pseudo error covariance for the jth Monte Carlo simulation, where $j = 1, \ldots, m$. Then we assess how *informative* [31] the state estimate $\hat{X}^{\mathrm{da}}_j(kh)$ is by evaluating the mean trace (MT) of $P^{\mathrm{da}}_j(kh)$ given by (21) and (29) over $[k_0, k_{\mathrm{f}}]$ and over m Monte Carlo simulations, that is,

$$\mathrm{MT} \triangleq \frac{1}{m}\sum_{j=1}^{m}\left[\frac{1}{k_{\mathrm{f}}-k_0+1}\sum_{k=k_0}^{k_{\mathrm{f}}}\mathrm{tr}\,P^{\mathrm{da}}(kh)\right]. \tag{38}$$

$$\mathcal{Y}_j(k) \triangleq [\,\mathcal{D}_1(k) \quad \cdots \quad \mathcal{D}_{p_k}(k) \quad \mathcal{A}_1(k) \quad \cdots \quad \mathcal{A}_{p_k}(k) \quad \mathcal{E}_1(k) \quad \cdots \quad \mathcal{E}_{p_k}(k)\,]^{\mathrm{T}}, \tag{35}$$

Note that MT quantifies the uncertainty in the estimate $\hat{X}^{\mathrm{da}}(kh)$.

Finally, we measure the *computational effort* of SDEKF and SDUKF needed to compute $\hat{X}^{\mathrm{da}}(kh)$ from $\hat{X}^{\mathrm{da}}((k-1)h)$. We present the average CPU processing time per time step h.

Initialization

To obtain $\hat{X}^{\mathrm{f}}(t)$ and $P^{\mathrm{f}}(t)$, we integrate (13), (14), (25), and (26) using the variable-step-size Runge-Kutta algorithm `ode45` of Matlab with tolerance set to 10^{-12}. This tolerance is necessitated by the pseudo error covariance propagation (26) between measurements. We test various values of $\hat{X}^{\mathrm{da}}(0)$ corresponding to values of the initial true-anomaly error. To enhance the stability of the filters [1], [2], [14], [16], we set $Q = 10^{-2} I_6$.

Furthermore, we initialize $P^{\mathrm{da}}(0)$ as the diagonal matrix $P^{\mathrm{da}}(0) = \mathrm{diag}(100, 100, 1, 1, 1, 0.1)$. In doing so, however, Figure 3(a) shows that convergence is not attained for SDEKF for initial true-anomaly errors larger than 90°. In fact, the third column of the linearized measurement map $\hat{C}(k)$ given by (15) for range-only measurements, representing the out-of-plane position component, is zero when the observing satellites are in an equatorial orbit and the out-of-plane position estimate $\hat{z}^{\mathrm{f}}(kh)$ is zero. Since the linearized measurement map is used to update the filter gain $K(k)$ and covariance $P^{\mathrm{da}}(kh)$, depending on the choice of $P^{\mathrm{da}}(0)$, the out-of-plane position estimate $\hat{z}^{\mathrm{f}}(kh)$ is unchanged at each time step regardless of the z-component of the target satellite's position. This difficulty is thus due to the lack of observability of the linearized dynamics.

However, by choosing $P^{\mathrm{da}}(0)$ to be the nondiagonal matrix $P^{\mathrm{da}}(0) = \mathrm{diag}(100, 100, 1, 1, 1, 0.1) + 10^{-2}\, 1_{6\times 6}$, both filters exhibit global convergence, that is, convergence is attained for all initial true-anomaly errors between ±180°; see Figure 3(b). For the remainder of this article, we use this choice of $P^{\mathrm{da}}(0)$.

Alternatively, we can overcome the convergence issue discussed above either by considering the case in which the geometry of the observing satellites is not entirely coplanar or by including angle (azimuth and elevation) measurements in addition to range data. Simulations (not included) show that, for these cases, no substantial improvement in the accuracy of the estimates is obtained over the case in which a nondiagonal $P^{\mathrm{da}}(0)$ is chosen.

To implement SDUKF, we set $\alpha = 1$, $\beta = 2$, and $\kappa = 0$. For further details, see [14].

Target Acquisition

We first consider the ability of SDEKF and SDUKF to acquire the target, that is, to locate the target despite initial position and velocity errors. We set the sample interval to be $h = 1$ s and introduce Gaussian measurement noise with a standard deviation of 0.1 km, which corresponds to $R = 0.01 I_6$ km^2 in (19) and (33). For initial estimates that are erroneous by 180°, Figure 4 shows that the SDUKF estimates are more accurate than the SDEKF estimates. This case is illustrated in Figure 3(b). The same

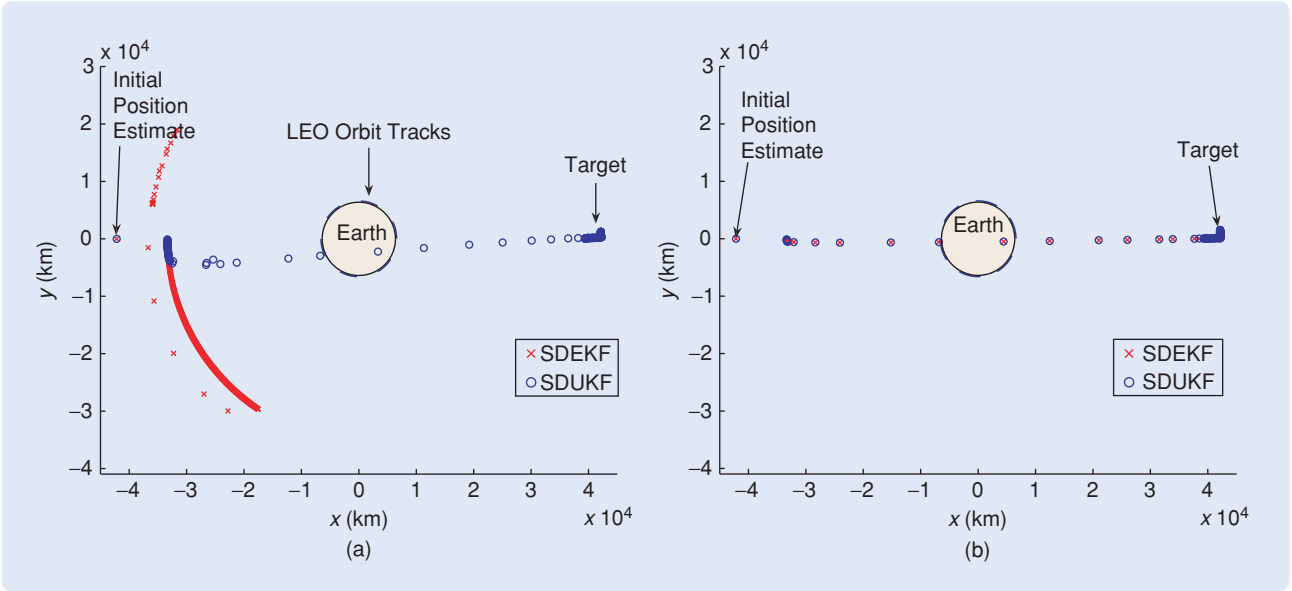

FIGURE 3 Sampled-data extended Kalman filter (SDEKF) and sampled-data unscented Kalman filter (SDUKF) target-position estimates × and ○, respectively, with an initial true-anomaly error of 180°. The initial location of the target is at 3:00. In (a), we set $P^{\mathrm{da}}(0) = \mathrm{diag}(100, 100, 1, 1, 1, 0.1)$, while in (b), we set a nondiagonal $P^{\mathrm{da}}(0) = \mathrm{diag}(100, 100, 1, 1, 1, 0.1) + 10^{-2}\, 1_{6\times 6}$. Range is measured with sample interval $h = 1$ s from six low-Earth-orbit (LEO) satellites (whose tracks are shown), and with Gaussian measurement noise whose standard deviation is 0.1 km and thus with $R = 0.01\, I_6$ km^2 in (19) and (33). SDEKF does not converge for case (a), while SDUKF approaches the vicinity of the target within about 300 s for case (a). Both SDEKF and SDUKF approach the target within about 250 s for case (b). The Earth and all LEO locations are drawn to scale.

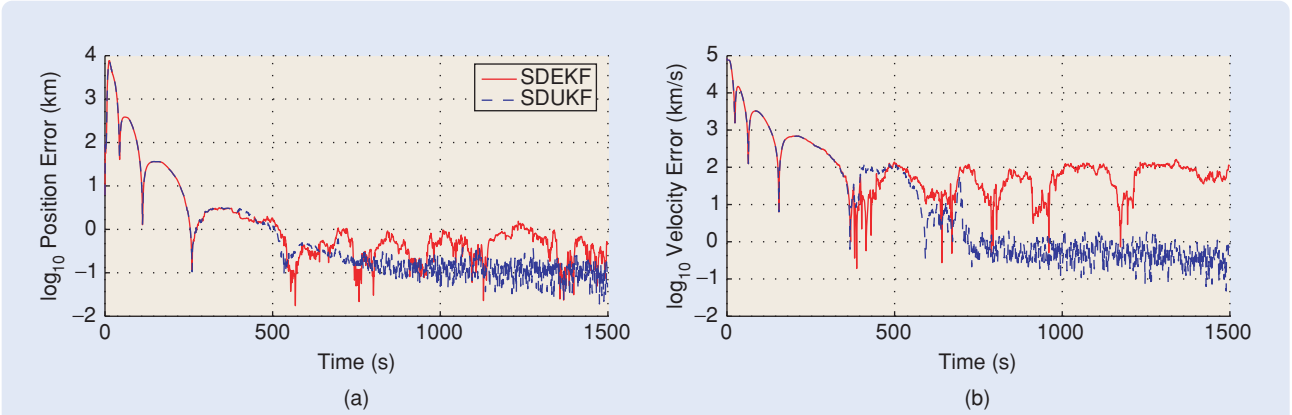

FIGURE 4 (a) Target position-estimate and (b) velocity-estimate errors with an initial true-anomaly error of 180° and nondiagonal $P^{\mathrm{da}}(0) = \mathrm{diag}(100, 100, 1, 1, 1, 0.1) + 10^{-2}\,1_{6\times 6}$. The range data are measured with sample interval $h = 1$ s from six LEO satellites, and with Gaussian measurement noise whose standard deviation is 0.1 km and thus with $R = 0.01\,I_6$ km^2 in (19) and (33). After 600 s, the sampled-data unscented Kalman filter (SDUKF) estimates are more accurate than the sampled-data extended Kalman filter (SDEKF) estimates. In particular, note that the SDUKF velocity estimates are two orders of magnitude more accurate than the SDEKF velocity estimates.

result (not shown) is verified for an initial true-anomaly error of −90°.

Based on a 100-run Monte Carlo simulation, Table 1 shows that SDUKF yields more accurate estimates for z and v_z than does SDEKF. However, the SDUKF processing time is about twice as large as the SDEKF processing time. Moreover, although SDUKF presents a larger value of MP (without accounting for the components z and v_z), which indicates less informative estimates, note that the SDEKF estimates for the position coordinate x do not remain inside the confidence interval defined by $\pm 3\sqrt{P^{\mathrm{da}}_{1,1}(kh)}$ [see Figure 5(a)], even with a larger value of Q. Consequently, $P^{\mathrm{da}}_{1,1}(kh)$ of SDEKF is not statistically consistent with the SDEKF x-error estimates.

Next we consider the ability of the filters to acquire the target under time-sparse range-only measurements with a measurement standard deviation of 0.1 km. For an initial true-anomaly error of 10°, Figure 6 shows the SDEKF and SDUKF position-estimate errors for $h = 1, 10, 50, 100, 600$ s. The SDUKF estimates are more accurate than the SDEKF estimates for all sample intervals investigated. Also, SDEKF does not converge for $h \geq 100$ s, whereas SDUKF converges for $h \leq 600$ s.

Finally, we consider the case in which six satellites in circular equatorial LEO at a radius of 6600 km are observing a target satellite in a polar orbit at a radius of 42,164 km. We set the sample interval to be $h = 1$ s and introduce Gaussian measurement noise with a standard deviation of 0.1 km. For an initial estimate that is erroneous by 180° in the argument of perigee, that is, $\hat{z}^{\mathrm{da}}(0) = -z(0)$ and $\hat{v}^{\mathrm{da}}_z(0) = -v_z(0)$, we compare the performance of SDEKF and SDUKF. For this example, we set $P^{\mathrm{da}}(0) = \mathrm{diag}\,(100, 100, 10^{10}, 1, 1, 0.1) + 10^{-2}\,1_{6\times 6}$, where $P^{\mathrm{da}}_{3,3}(0)$ is set to a large value to reflect the large initial uncertainty in z. Because of the polar orbit, the range-only output map from all of the observing spacecraft has even symmetry, and thus ambiguity can occur. Figure 7 shows that SDUKF approaches the vicinity of the target within about 30 s, while SDEKF converges to the mirror image of the z-position component.

TABLE 1 RMSE$_i$, mean trace (MT), and average CPU processing time for $t \in [500, 1500]$ s and for a 100-run Monte Carlo simulation using the sampled-data extended Kalman filter (SDEKF) and the sampled-data unscented Kalman filter (SDUKF). Range is measured with sample interval $h = 1$ s from six low-Earth-orbit satellites and with Gaussian measurement noise whose standard deviation is 0.1 km. All initial estimates are erroneous by −90°. $P^{\mathrm{da}}_{3,3}$ and $P^{\mathrm{da}}_{6,6}$ are not included in the calculation of MT because their values are much greater than the remaining diagonal entries.

	RMSE$_i$					
	x (km)	y (km)	z (km)	v_x (km/s)	v_y (km/s)	v_z (km/s)
SDEKF	0.1128	0.2996	63.93	0.0351	0.0841	0.5149
SDUKF	0.5525	0.3175	13.80	0.0958	0.0849	0.2450
	MT (excluding $P^{\mathrm{da}}_{3,3}$ and $P^{\mathrm{da}}_{6,6}$)					
SDEKF	0.1661					
SDUKF	0.5998					
	Average CPU processing time (ms)					
SDEKF	19.5					
SDUKF	41.8					

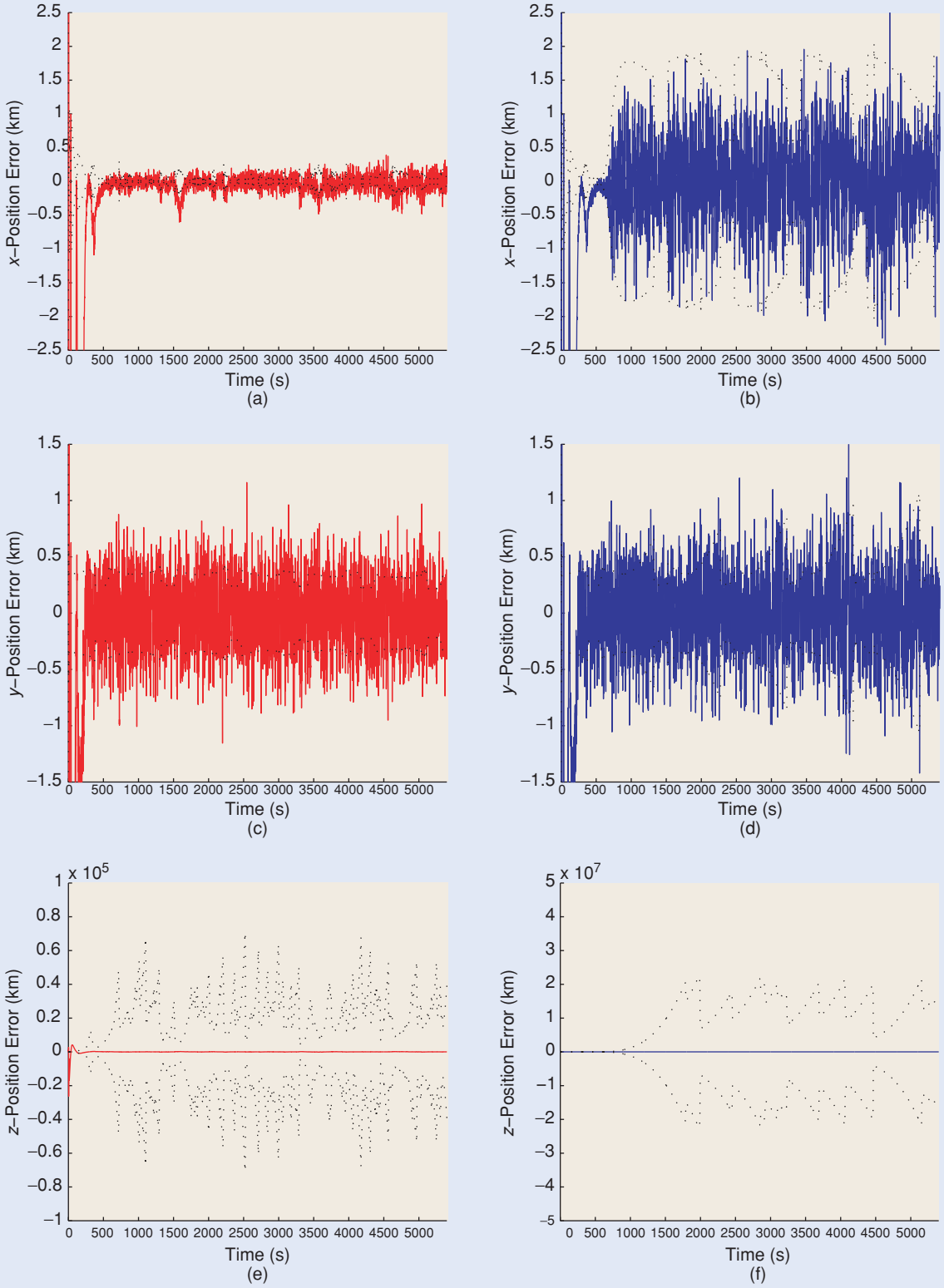

FIGURE 5 Target x, y, and z position-estimate errors (——) around the confidence interval $(\cdots)$ defined by $\pm 3\sqrt{P^{\mathrm{da}}_{1,1}(kh)}$, $\pm 3\sqrt{P^{\mathrm{da}}_{2,2}(kh)}$, and $\pm 3\sqrt{P^{\mathrm{da}}_{3,3}(kh)}$, respectively. (a), (c), and (e) refer to sampled-data extended Kalman filter estimates, while (b), (d), and (f) refer to sampled-data unscented Kalman filter estimates. We consider an initial true-anomaly error of -90°. The range data are measured with sample interval $h = 1$ s from six low-Earth-orbit satellites, and with Guassian measurement noise whose standard deviation is 0.1 km. As shown in (e) and (f), the z–position error is close to zero. However, due to a lack of observability, $P^{\mathrm{da}}_{3,3}(kh)$ becomes large.

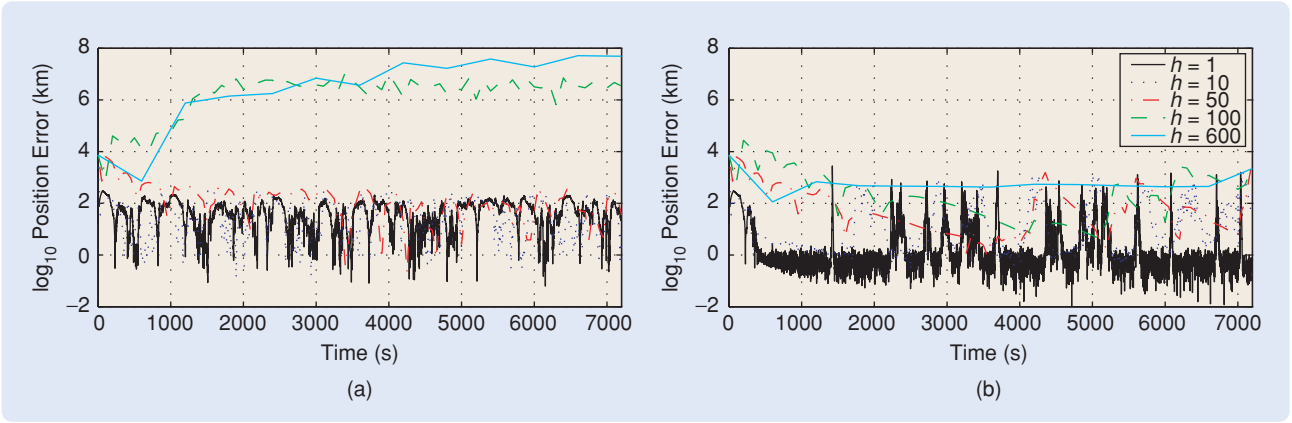

FIGURE 6 (a) Sampled-data extended Kalman filter (SDEKF) and (b) sampled-data unscented Kalman filter (SDUKF) target position-estimate errors for sample intervals $h = 1, 10, 50, 100, 600$ s with range measurements from six low-Earth-orbit satellites with measurement-noise standard deviation of 0.1 km, that is, $R = 0.01\, I_6$ km^2. The SDUKF estimates are more accurate than the SDEKF estimates for all sample intervals investigated. Also, SDEKF does not converge for $h \geq 100$ s.

Intermeasurement Tracking Accuracy

Next, we assess the ability of SDEKF and SDUKF to track the target along an equatorial orbit. To see how the position and velocity estimates degrade between data updates, we consider an initial true-anomaly error of -30° and a sample interval of $h = 50$ s with measurement noise having a standard deviation of 0.1 km, that is, $R = 0.01\, I_6$ km^2. Figure 8 shows the growth of the position and velocity errors between range-only measurements as well as the position and velocity error reduction that occurs due to data injection.

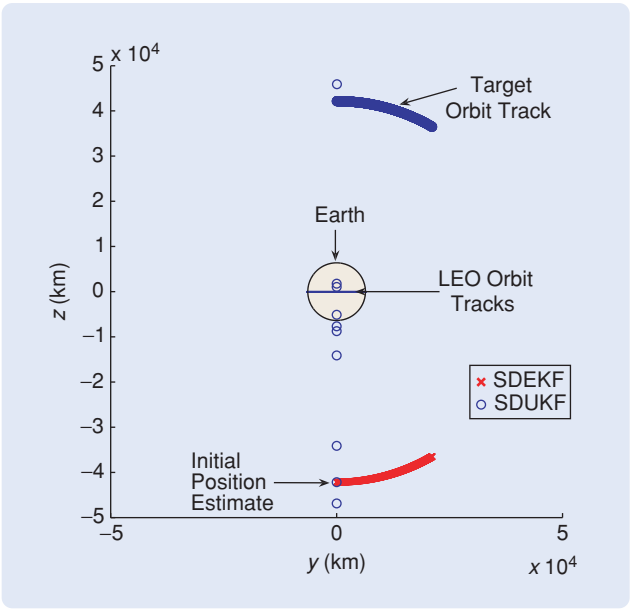

FIGURE 7 Sampled-data extended Kalman filter (SDEKF) and sampled-data unscented Kalman filter (SDUKF) target-position estimates $\times$ and $\circ$, respectively. The initial location of the target is above the North Pole in a polar orbit, but we initialize both filters with an initial argument-of-perigee error of 180°, that is, over the South Pole. We set $P^{\mathrm{da}}(0) = \mathrm{diag}(100, 100, 10^{10}, 1, 1, 0.1) + 10^{-2}\, 1_{6\times 6}$. Range is measured with sample interval $h = 1$ s from six low-Earth-orbit (LEO) satellites (whose tracks are shown), and with Gaussian measurement noise whose standard deviation is 0.1 km. SDUKF approaches the vicinity of the target within about 30 s, while SDEKF converges to the mirror image of the z-position state. The Earth and all LEO locations are drawn to scale. We note that both filters fail to acquire the target when $P^{\mathrm{da}}(0) = \mathrm{diag}(100, 100, 10^{10}, 1, 1, 0.1)$.

Eccentricity Estimation

We now consider the case in which the target performs an unknown thrust maneuver that changes the eccentricity of its orbit. In particular, the target is initially in a circular orbit as in the previous examples. At time $t = 1000$ s, the target performs a 1-s burn that produces a specific thrust (that is, acceleration) $w = [0\ 0.5\ 0]^{\mathrm{T}}$ km/s^2, while, at time $t = 1500$ s, the target performs a 1-s burn that produces a specific thrust $w = [0\ 0.3\ 0]^{\mathrm{T}}$ km/s^2. With an initial eccentricity of $e = 0$, corresponding to a circular orbit, the eccentricity after the first burn is $e \approx 0.35$, while the eccentricity after the second burn is $e \approx 0.59$. The initial true-anomaly error is set to -30°. Assuming measurement noise with a standard deviation of 0.1 km, that is, $R = 0.01\, I_6$ km^2, along with range-only measurements available with a sample interval of $h = 10$ s, the SDEKF and SDUKF eccentricity estimates are shown in Figure 9.

For a 100-run Monte Carlo simulation, we obtain RMSE indices of 0.0862 and 0.0731, respectively, for the eccentricity estimates using SDEKF and SDUKF over $t \in [500, 2500]$ s. These indices indicate that SDUKF yields more accurate eccentricity estimates than does SDEKF.

Inclination Estimation with Range-Only Measurements

We now consider the case in which the target performs an unknown thrust maneuver that changes its inclination. The target is initially in a circular orbit with inclination $i = 0$ rad. At time $t = 3000$ s, the target performs a 1-s burn that produces a specific thrust $w = [0\ 0\ 0.5]^{\mathrm{T}}$ km/s^2, while, at time $t = 5000$ s, the target performs a 1-s burn that

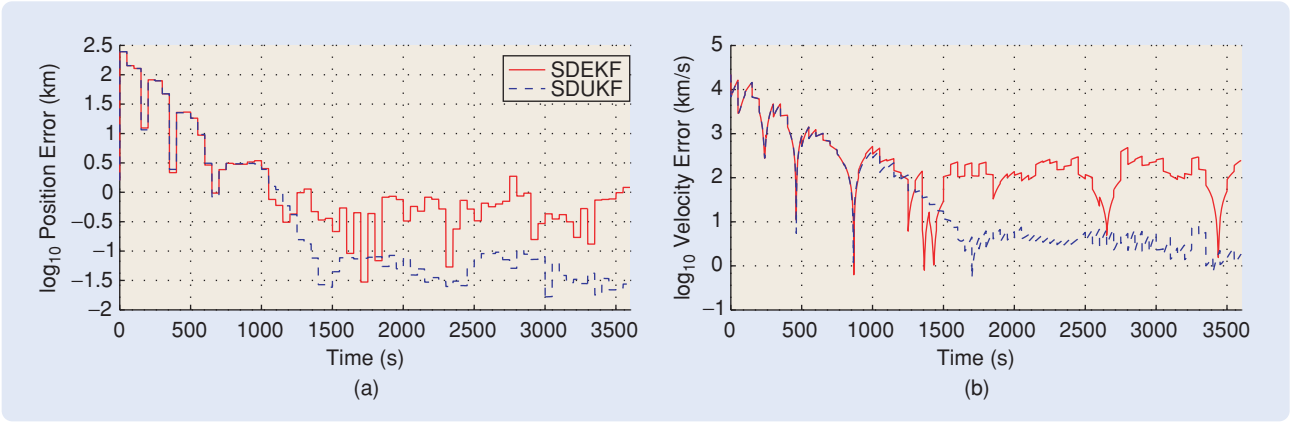

FIGURE 8 (a) Target position-estimate and (b) velocity-estimate errors with an initial true-anomaly error of -30°, sample interval $h = 50$ s, and range measurements with measurement-noise standard deviation of 0.1 km, that is, $R = 0.01\, I_6$ km^2. The position-estimate error between measurements slowly grows with time and thus is not discernible in (a). The growth of the velocity-estimate error between measurements can be seen as well as the position and velocity-error reduction that occurs due to data injection. The sampled-data unscented Kalman (SDUKF) filter estimates are more accurate than the sampled-data extended Kalman filter (SDEKF) estimates.

produces a specific thrust $w = [0\ 0\ -0.2]^{\mathrm{T}}$ km/s^2. The inclination after the first burn is $i \approx 0.16$ rad, whereas the inclination after the second burn is $i \approx 0.097$ rad. We assume range-only measurements with measurement-noise standard deviation of 0.032 km, and assume an initial true-anomaly error of -30°. For numerical conditioning, we set $R = 0.01\, I_6$ km^2. The SDEKF and SDUKF inclination estimates are shown in Figure 10(a). After an initial transient, SDEKF is able to track changes in the target's inclination. On the other hand, even though SDUKF yields more accurate estimates over $t \in [0, 3000]$ s, SDUKF yields erroneous inclination estimates close to zero after the target's maneuver. In this case, unlike SDEKF, SDUKF yields highly biased estimates for the position z for $t > 3000$ s.

The inability of SDUKF to detect changes in the inclination due to the target's maneuvers can also be overcome by initializing the estimated inclination to a small nonzero value, specifically, -0.1 rad. However, if the estimate converges to zero, then the filter can fail to detect further changes in the target's inclination. Alternatively, we can slightly alter the inclination of the observing satellites so that the geometry is not entirely coplanar. We thus change the orbit of two observing satellites by giving them an inclination of -0.1 rad and -0.2 rad, respectively. After an initial transient (from $t = 3000$ s to $t = 3200$ s), Figure 10(b) shows the ability of both filters to track the true inclination, despite an initial inclination estimate of 0 rad. Note that, according to Figure 10(b), SDEKF yields less accurate inclination estimates than SDUKF over $t \in [0, 3000]$ s.

Inclination Estimation with Range and Angle Measurements

With all six observing satellites in an equatorial orbit, the target performs an unknown thrust maneuver that changes its inclination as in the previous subsection. We now augment the range measurements with angle (azimuth and elevation) data. We assume range and angle measurement-noise standard deviations of 0.032 km and 0.032 rad, respectively, and assume an initial true-anomaly error of -30° with all remaining parameters as in Figure 10. For numerical conditioning, we set $R = \mathrm{diag}\,(0.01\, I_6$ km^2, $0.001\, I_{12}$ rad$^2)$. The inclination estimates obtained from SDEKF and SDUKF are shown in Figure 11(a).

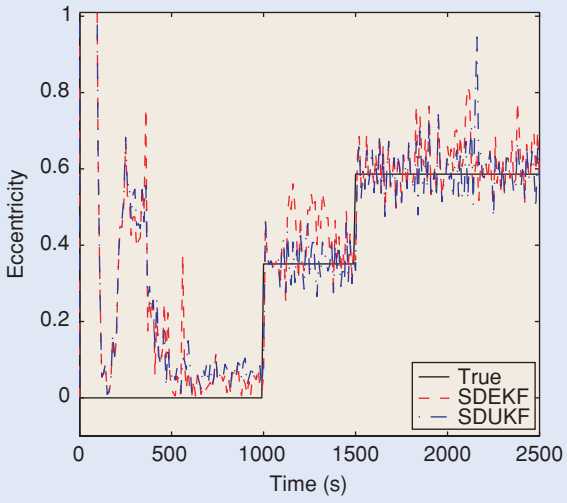

FIGURE 9 Estimated eccentricity with the sample interval $h = 10$ s, with an initial true-anomaly error of -30°, and with range measurements having measurement-noise standard deviation of 0.1 km, that is, $R = 0.01\, I_6$ km^2. The target performs unknown 1-s burns at $t = 1000$ s and $t = 1500$ s. The initial eccentricity is $e = 0$, corresponding to the initial circular orbit, while the eccentricity after the first burn is $e \approx 0.35$, and the eccentricity after the second burn is $e \approx 0.59$. These results show the sensitivity of the eccentricity estimates to measurement noise.

Figure 11(a) shows that, after the orbital maneuver, the filters track the inclination changes. The addition of angle measurements enables SDUKF to detect changes in the target's inclination. Moreover, Figure 11(b) shows that, when the geometry of the observing satellites is not entirely coplanar [as in Figure 10(b)] and angle measurements are used in addition to range data, the inclination estimates are more accurate than the estimates shown in Figure 10(a).

Table 2 compares the performance of SDEKF and SDUKF for the case in which the target is maneuvering such that its inclination changes, $h = 1$, and the initial true-anomaly error is -30°. We consider a 100-run Monte

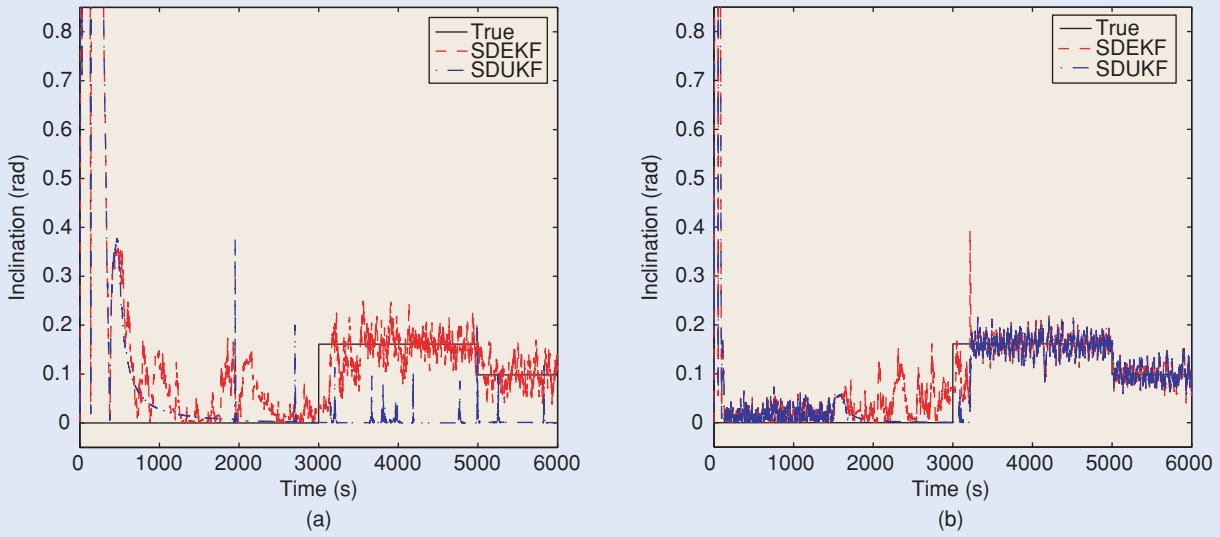

FIGURE 10 Estimated inclination with the sample interval $h = 1$ s, with an initial true-anomaly error of -30°, and with range measurements having measurement-noise standard deviation 0.032 km. In (a), the sampled-data unscented Kalman filter (SDUKF) fails by getting stuck in estimating $i \approx 0$, while the sampled-data extended Kalman filter (SDEKF) detects changes in the target's inclination. In (b), we slightly change the orbit of two observing satellites by giving them inclinations of -0.1 rad and -0.2 rad, respectively. After an initial transient, both filters provide improved estimates of the target's inclination.

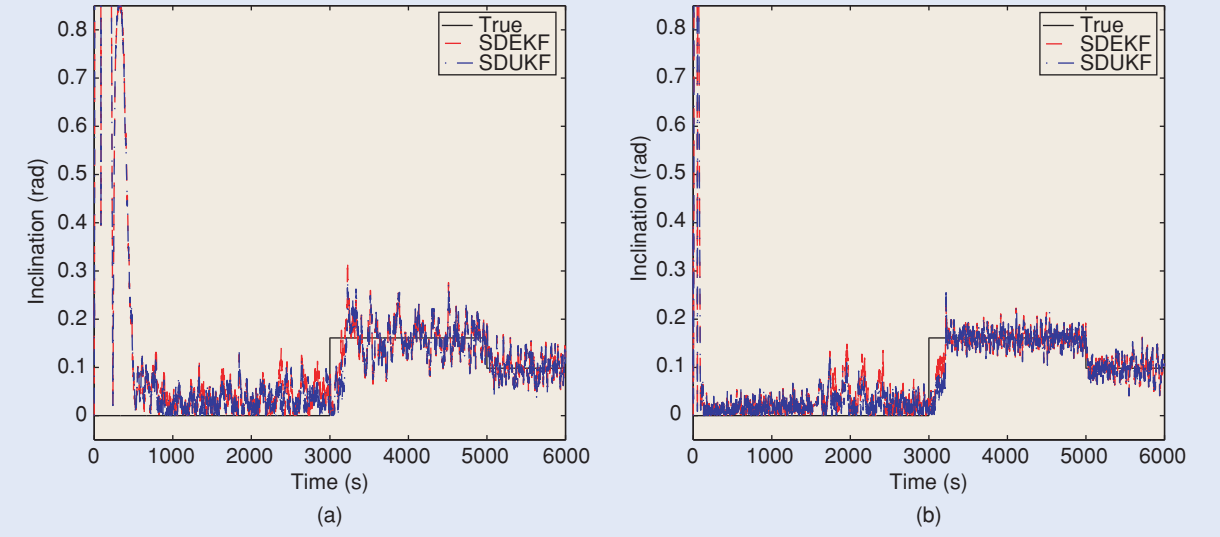

FIGURE 11 (a) Estimated inclination with the sample interval $h = 1$ s, with an initial true-anomaly error of -30° and range and angle measurement-noise standard deviations of 0.032 km and 0.032 rad, respectively. In (b), we slightly change the orbit of two observing satellites by giving them inclinations of -0.1 rad and -0.2 rad, respectively. In both cases, angle (azimuth and elevation) measurements in addition to range measurements from the observing satellites allow the sampled-data extended Kalman filter (SDEKF) and the sampled-data unscented Kalman filter (SDUKF) to detect changes in the target's inclination.

Carlo simulation where i) range-only measurements are used, ii) range-only measurements are used together with noncoplanar observing satellites, iii) range and angle measurements are used, and iv) range and angle measurements are used together with noncoplanar observing satellites. Comparing the indices RMSE_i, we observe that SDUKF outperforms SDEKF for z and v_z, SDEKF outperforms SDUKF for x and v_x, and the filters have similar accuracy for y and v_y. Regarding the inclination estimates, except for case i) for which SDUKF fails to track the inclination changes, SDUKF yields more accurate estimates than SDEKF. Also, with the inclusion of angle measurements, both filters yield similar MT indices. Moreover, the SDUKF processing time is twice as long as the SDEKF processing time.

CONCLUSIONS

The goal of this article is to illustrate and compare two algorithms for nonlinear sampled-data state estimation. Under idealized assumptions on the astrodynamics of bodies orbiting the Earth, we apply SDEKF and SDUKF for range-only as well as range and angle observations provided by a constellation of six LEO satellites in circular, equatorial orbits. We study the ability of the filters to acquire and track a target satellite in geosynchronous orbit as a function of the sample interval, initial uncertainty, and type of available measurements.

For target acquisition, SDUKF yields more accurate position and velocity estimates than SDEKF. Moreover, the convergence of SDEKF is sensitive to the initialization of the error covariance; in fact, a nondiagonal initial covariance is found to be more effective than a diagonal initial covariance. Like SDUKF, by properly setting a nondiagonal initial error covariance, SDEKF also exhibits global convergence, that is, convergence is attained for all initial true-anomaly errors. However, when the target is in a polar orbit and the observing satellites are in an equatorial orbit, unlike SDUKF, SDEKF does not converge for an initial argument-of-perigee error of 180°. In this case, SDEKF yields z-position estimates that are the mirror image of the true value.

Under time-sparse range-only measurements, SDEKF is not able to track the target for a time step $h \geq 100$ s. On the other hand, the SDUKF estimates converge for $h \leq 600$ s.

TABLE 2 RMSE_i, mean trace (MT), and average CPU processing time for $t \in [500, 6000]$ s and for a 100-run Monte Carlo simulation using the sampled-data extended Kalman filter (SDEKF) and the sampled-data unscented Kalman filter (SDUKF). The target is maneuvering such that its inclination changes, $h = 1$ s, and the initial true-anomaly error is $-30°$. We consider the following cases: i) range-only measurements are used, ii) range-only measurements are used with the geometry of the observing satellites not entirely coplanar, iii) range and angle measurements are used, and iv) range and angle measurements are used with the geometry of the observing satellites not entirely coplanar.

		RMSE_i						
		x (km)	y (km)	z (km)	v_x (km/s)	v_y (km/s)	v_z (km/s)	i (rad)
SDEKF	i)	0.0653	0.0957	613.6	0.0128	0.0261	0.4369	0.0658
	ii)	0.0648	0.1158	22.78	0.0133	0.0263	0.1478	0.0389
	iii)	0.0610	0.0953	18.47	0.0128	0.0261	0.1808	0.0562
	iv)	0.0630	0.1154	12.57	0.0130	0.0262	0.1205	0.0372
SDUKF	i)	0.2573	0.1313	605.7	0.0341	0.0276	0.3392	0.1080
	ii)	0.1279	0.1193	17.38	0.0210	0.0266	0.1142	0.0355
	iii)	0.0900	0.0965	14.30	0.0113	0.0260	0.1560	0.0485
	iv)	0.0805	0.1160	10.38	0.0121	0.0262	0.1116	0.0344
		MT (excluding $P^{\text{da}}_{3,3}$ and $P^{\text{da}}_{6,6}$)						
SDEKF	i)	0.2057						
	ii)	0.2621						
	iii)	0.2013						
	iv)	0.2601						
SDUKF	i)	0.7229						
	ii)	0.4190						
	iii)	0.2239						
	iv)	0.2734						
		Average CPU processing time (ms)						
SDEKF	i)	20.4						
	ii)	20.5						
	iii)	20.3						
	iv)	20.9						
SDUKF	i)	38.6						
	ii)	39.2						
	iii)	38.5						
	iv)	39.7						

When the target is maneuvering such that its eccentricity changes, SDUKF tracks the target's eccentricity more accurately than SDEKF.

Unlike SDEKF, SDUKF is not able to detect changes in the target's inclination when the target is maneuvering. Nevertheless, either by having the observing satellites not entirely coplanar or by including angle measurements, convergence is attained for both filters. Furthermore, when angle measurements are also available, SDUKF yields more accurate inclination estimates than SDEKF. Finally, the SDUKF processing time is about twice the SDEKF processing time.

REFERENCES

[1] A.H. Jazwinski, *Stochastic Processes and Filtering Theory*. New York: Academic, 1970.

[2] *Applied Optimal Estimation*, A. Gelb, Ed. Cambridge, MA: MIT Press, 1974.

[3] F.E. Daum, "Exact finite-dimensional nonlinear filters," *IEEE Trans. Automat. Contr.*, vol. 31, pp. 616–622, 1986.

[4] F.E. Daum, "Nonlinear filters: Beyond the Kalman filter," *IEEE Aerosp. Elec. Sys. Mag.*, vol. 20, pp. 57–69, 2005.

[5] A.J. Krener and W. Respondek, "Nonlinear observers with linearizable error dynamics," *SIAM J. Contr. Optim.*, vol. 23, pp. 197–216, 1985.

[6] P.E. Moraal and J.W. Grizzle, "Observer design for nonlinear systems with discrete-time measurements," *IEEE Trans. Autom. Contr.*, vol. 40, pp. 395–404, 1995.

[7] S. Bolognani, L. Tubiana, and M. Zigliotto, "Extended Kalman filter tuning in sensorless PMSM drives," *IEEE Trans. Ind. Appl.*, vol. 39, pp. 1741–1747, 2003.

[8] S. Carme, D.-T. Pham, and J. Verron, "Improving the singular evolutive extended Kalman filter for strongly nonlinear models for use in ocean data assimilation," *Inverse Problems*, vol. 17, pp. 1535–1559, 2001.

[9] M. Boutayeb, H. Rafaralahy, and M. Darouach, "Convergence analysis of the extended Kalman filter used as an observer for nonlinear deterministic discrete-time systems," *IEEE Trans. Automat. Contr.*, vol. 42, pp. 581–586, 1997.

[10] K. Reif, S. Gunther, E. Yaz, and R. Unbehauen, "Stochastic stability of the discrete-time extended Kalman filter," *IEEE Trans. Automat. Contr.*, vol. 44, pp. 714–728, 1999.

[11] K. Reif, S. Gunther, E. Yaz, and R. Unbehauen, "Stochastic stability of the continuous-time extended Kalman filter," *IEE Proc. Control Theory Appl.*, vol. 147, pp. 45–52, 2000.

[12] K. Xiong, H.Y. Zhang, and C.W. Chan, "Performance evaluation of UKF-based nonlinear filtering," *Automatica*, vol. 42, pp. 261–270, 2006.

[13] K. Xiong, H.Y. Zhang, and C.W. Chan, "Author's reply to 'comments on performance evaluation of UKF-based nonlinear filtering,'" *Automatica*, vol. 43, pp. 569–570, 2007.

[14] S.J. Julier and J.K. Uhlmann, "Unscented filtering and nonlinear estimation," *Proc. IEEE*, vol. 92, pp. 401–422, Mar. 2004.

[15] S. Julier, J. Uhlmann, and H.F. Durrant-Whyte, "A new method for the nonlinear transformation of means and covariances in filters and estimators," *IEEE Trans. Automat. Contr.*, vol. 45, pp. 477–482, 2000.

[16] S. Särkkä, "On unscented Kalman filtering for state estimation of continuous-time nonlinear systems," *IEEE Trans. Automat. Contr.*, vol. 52, pp. 1631–1641, 2007.

[17] P.L. Houtekamer and H.L. Mitchell, "Data assimilation using an ensemble Kalman filter technique," *Monthly Weather Rev.*, vol. 126, pp. 796–811, 1998.

[18] G. Evensen, *Data Assimilation: The Ensemble Kalman Filter*. New York: Springer-Verlag, 2006.

[19] B.D. Tapley, B.E. Schutz, and G.H. Born, *Statistical Orbit Determination*, Elsevier, Amsterdam, 2004.

[20] D. Brouwer and G.M. *Clemence, Methods of Celestial Mechanics*. New York: Academic, 1961.

[21] N. Duong and C.B. Winn, "Orbit determination by range-only data," *J. Spacecraft Rockets*, vol. 10, pp. 132–136, 1973.

[22] V.L. Pisacane, R.J. Mcconahy, L.L. Pryor, J.M. Whisnant, and H.D. Black, "Orbit determination from passive range observations," *IEEE Trans. Aerosp. Electron. Syst.*, vol. 10, pp. 487–491, 1974.

[23] J.L. Fowler and J.S. Lee, "Extended Kalman filter in a dynamic spherical coordinate system for space based satellite tracking," in *Proc. AIAA 23rd Aerospace Sciences Meeting*, paper AIAA-85-0289, Reno, NV, 1985, pp. 1–7.

[24] D.J. Lee and K.T. Alfriend, "Sigma-point filtering for sequential orbit estimation and prediction," *J. Spacecraft Rockets*, vol. 44, pp. 388–398, 2007.

[25] D.E. Bizup and D.E. Brown, "Maneuver detection using the radar range rate measurement," *IEEE Trans. Aerosp. Electron. Syst.*, vol. 40, pp. 330–336, 2004.

[26] D.A. Cicci and G.H. Ballard, "Sensitivity of an extended Kalman filter 1. variation in the number of observers and types of observations," *Appl. Math. Comput.*, vol. 66, pp. 233–246, 1994.

[27] D.A. Cicci and G.H. Ballard, "Sensitivity of an extended Kalman filter 2. variation in the observation error levels, observation rates, and types of observations," *Appl. Math. Comput.*, vol. 66, pp. 247–259, 1994.

[28] D.S. Bernstein, "Newton's frames," *IEEE Contr. Syst. Mag.*, vol. 28, pp. 17–18, Feb. 2008.

[29] H.D. Curtis, *Orbital Mechanics for Engineering Students*. Amsterdam, The Netherlands: Elsevier, 2005.

[30] W. Sun, K. Nagpal, M. Krishan, and P. Khargonekar, "Control and filtering for sampled-data systems," *IEEE Trans. Automat. Contr.*, vol. 38, pp. 1162–1175, 1993.

[31] T. Lefebvre, H. Bruyninckx, and J. De Schutter, "Kalman filters for nonlinear systems: A comparison of performance," *Int. J. Contr.*, vol. 77, pp. 639–653, 2004.

[32] J.L. Crassidis, "Sigma-point Kalman filtering for integrated GPS and inertial navigation," *IEEE Trans. Aerosp. Electron. Syst.*, vol. 42, pp. 750–756, 2006.

AUTHOR INFORMATION

Bruno O.S. Teixeira (brunoot@ufmg.br) received the B.S. in control and automation engineering in 2004 and the Doctor degree in electrical engineering in 2008, both from the Federal University of Minas Gerais, Brazil. He was a visiting scholar (sponsored by CNPq – Brazil) in the Aerospace Engineering Department at the University of Michigan in 2006–2007. His interests are in state estimation, system identification, and control for aeronautical and aerospace applications. He can be contacted at the Graduate Program in Electrical Engineering–PPGEE, Federal University of Minas Gerais–UFMG, Av. Antônio Carlos, 6627, Pampulha, Belo Horizonte, MG, Brazil, 30.270-010.

Mario A. Santillo received the B.S. from Rensselaer Polytechnic Institute in aeronautical and mechanical engineering. He is currently a Ph.D. candidate in the Aerospace Engineering Department at the University of Michigan. His interests are in the areas of estimation and adaptive control for aerospace applications.

R. Scott Erwin received the Ph.D. from the University of Michigan. He is currently the technical area lead for Command, Control, and Communications (C^3) at the Air Force Research Laboratory's Space Vehicles Directorate (AFRL/RV), located at Kirtland Air Force Base in Albuquerque, New Mexico. His research interests include structural dynamics as well as spacecraft guidance, navigation, and control.

Dennis S. Bernstein received the Ph.D. from the University of Michigan, where he is a professor in the Aerospace Engineering Department. He is the author of *Matrix Mathematics* published by Princeton University Press. His interests are in system identification and adaptive control for aerospace applications.